1   **Using nanoindentation to quantify the mechanical profile of Wufeng-Longmaxi**

2   **Formation in Southwest China: Link to sedimentary conditions**

3   Jianfeng Wang [a, c*], Chao Yang [b**], Yuke Liu [d], Wenmin Jiang [a], Yun Li [a], Ting Zhang [e, f], Yijun

4   Zheng [a], Yuhong Liao [a], Qiuli Huo [g, h, i], Li Fu [g, h, i], Yusheng Wang [g, h, i], Ping'an Peng [a], Yongqiang

5   Xiong [a]

6   a. State Key Laboratory of Deep Earth Processes and Resources, Guangzhou Institute of

7   Geochemistry, Chinese Academy of Sciences, Guangzhou 510640, *PR* China

8   b. Guangzhou Institute of Energy Conversion, Chinese Academy of Sciences, Guangzhou 510640,

9   *PR* China

10   c. The Njord Centre, Departments of Geosciences and Physics, University of Oslo, Blindern, 0316

11   Oslo, Norway

12   d. Research Institute of Petroleum Exploration and Development, Beijing 100083, *PR* China

13   e. Key Laboratory of Petroleum Resources Research, Gansu Province, Lanzhou 730000, *PR* China

14   f. Research Center for Oil and Gas Resources, Northwest Institute of Eco-Environment and

15   Resources, Chinese Academy of Sciences, Lanzhou 730000, *PR* China

16   g. Exploration and Development Research Institutle of PetroChina Daqing Oilfield Co., Ltd.,

17   Daqing 163712, *PR* China

18   h. State Key Laboratory of Continental Shale Oil, Daqing, 163712, *PR* China

19   i. Heilongjiang Provincial Key laboratory of Continental Shale Oil, Daqing, 163712, *PR* China

20   * Corresponding Authors: Jianfeng Wang; wangjianfeng@gig.ac.cn;

21   Chao Yang; yangchao@ms.giec.ac.cn

Abstract

The fine construction of a continuous mechanical profile for the Wufeng to Longmaxi (WF-LMX) Formation sequence is crucial for designing hydraulic fracturing projects in shale gas development. However, the microscale mechanical profile of WF-LMX Formation shale and its relationship to sedimentary conditions are poorly understood. This study investigates the mechanical profile of the WF-LMX Formation sequence using nanoindentation. A total of 27 cutting samples were collected at one to one-half meter intervals from the Sanquan-1 well. Nanoindentation testing, rock mineralogy, major element analysis, and porosimetry were performed. The results showed that the WF-LMX shales in this study region were deposited in a passive continental margin environment, primarily from biogenic silica. Mechanical properties (hardness, fracture toughness, Young's modulus, and brittle index) varied synchronously with mineral and organic content across the vertical drilling profile, reflecting changes in lithology and sedimentary facies within the WF-LMX Formation. Shales in the upper part of the WF Formation and lower part of the LMX Formation, belonging to the deep-water shelf facies, exhibited high mechanical properties. Quartz and clay play a dominant role in controlling shale mechanics, while the minor rock constituents, nanoporosity have little effect. In particular, biogenic silica (authigenic quartz) plays an important role in increasing the brittleness of shale. The effect of shale constituents on micromechanics is essentially controlled by the sedimentary environment. Additionally, the potential of using nanoindentation to effectively assess shale brittleness was also demonstrated. This study provides a continuous and accurate interpretation profile of mechanical parameters and is helpful in determining favorable intervals for hydraulic fracturing in the design of shale gas development.

44   **Keywords:** Wufeng-Longmaxi Formation shale, sedimentary environment, mechanical profile,

45   mineralogy, nanoindentation

1 Introduction

48   Shale gas is a significant unconventional hydrocarbon resource in China, and occurs in

49   shale-dominated formations with low porosity and low permeability (Zou et al., 2010). Realizing

50   commercial development of shale gas requires large-scale reservoir fracturing of shale formations

51   (Guo et al., 2014). The optimal design of reservoir stimulation (i.e., hydraulic fracturing) highly

52   depends on the reliable measurement of the mechanics of shale at different scales, which remains

53   an ongoing challenge (Rickman et al., 2008, Sone and Zoback 2013a, b). In the past, the

54   uniaxial/triaxial compression and the acoustic emission tests were the most common methods to

55   investigate the mechanical properties of shale rock. These tests are conducted on centimeter-sized

56   cores, thus obtaining shale mechanics at core scale. Although these macroscopic mechanical

57   testing methods can provide reliable and directly applicable rock mechanics data for exploration

58   and development, they are always flawed, especially when mechanical characterization of the

59   entire shale formation is required to optimize favorable fracture intervals, since they rely on bulky

60   core samples that are typically difficult to obtain (Alramahi and Sundberg 2012, Sone and Zoback

61   2013a).

62   Nanoindentation, a technique widely used in micromechanical characterization, is

63   increasingly being used to evaluate the micromechanical properties of shales (Ulm et al., 2005). It

64   involves pressing a hard needle tip to press into the surface of the material, thus requiring small

65   sample volumes on the millimeter scale. Because drill cuttings (at the millimeter scale) can meet

66   the requirements of nanoindentation mechanical testing and are readily available, the

67   nanoindentation can achieve accurate mechanical characterization of the entire shale formation.

68   By adjusting the indentation depth or applied load, elastic-plastic parameters such as hardness and

69   Young's modulus of materials can be quickly derived from the load-displacement curves (Oliver

70   and Pharr 1992). In addition, by developing mathematical models, scholars have also used

71   indentation data to calculate other mechanical parameters, including fracture toughness

72   characterizing the ability of a material to resist crack propagation, and brittleness index

73   quantifying the fracturability of materials (Lawn and Marshall 1979, Ma et al. 2023). In order to

74   determine the micromechanical properties of shales by nanoindentation, it is crucial to develop an

75   appropriate indentation protocol, highlighting the importance of establishing a well-designed

76   approach in this field, because shales have a more pronounced size effect and transverse

77   heterogeneity at the microscale (Ulm and Abousleiman 2006, Wang et al., 2022a, 2023, Yang et al.,

78   2020). Currently, a statistical grid nanoindentation scheme is widely used, which is based on

79   averaging a large amount of mechanical data from a series of indentations performed over a

80   sufficiently large area and using large indentation loads (200-500 mN) (Abedi et al., 2016, Gupta

81   et al., 2018, 2020, Kumar et al., 2012, Long et al., 2021, Shi et al., 2019a, 2019b, 2020, Shukla et

82   al., 2013, Zhao et al., 2019). The use of a relatively large load is to indent a large volume to

83   involve more matrix phases in each indentation (i.e., to reduce the impact of size effects), and the

84   use of a nanoindentation campaign is to make the results more statistically significant (i.e., to

85   reduce the impact of heterogeneity). A large number of indentation cases indicate that this method

86   is reliable and scientific for obtaining the micromechanical properties of shale. Besides, some

87   research indicates that the Young's modulus determined by acoustic emission testing correlates

88 well with measurements obtained by nanoindentation (Kumar et al., 2012). In general, the

89 mechanical properties (mainly Young's modulus) measured by nanoindentation can provides us

90 with an efficient approach to analyze the mechanical properties and variation patterns of specific

91 shale formation at the microscopic scale.

92 The Wufeng-Longmaxi (WF-LMX) Formation shales are the primary marine formations for

93 shale gas exploration and development in southern China, with commercial developments

94 successfully implemented in several locations including Fuling, Changning, and Weiyuan in

95 Sichuan Province, China (Zou et al., 2010). In particular, the marine black shales of the WF-LMX

96 Formation were predominantly deposited in a deep-water shelf environment characterized by

97 strong reducing conditions (Zou et al., 2010). To date, extensive research has been conducted and

98 documented on the geologic characteristics of areas conducive to WF-LMX shale gas

99 accumulation (Guo and Zeng 2015, Yan et al., 2018, Zheng et al., 2022, Zou et al., 2010).

100 Currently, engineering challenges have emerged as critical to the success of shale gas development.

101 Among these, rock mechanics research, particularly as it relates to hydraulic fracturing, has been

102 at the forefront of research efforts. Previous mechanical research on the WF-LMX shale was

103 mainly based on macromechanical testing (Guo et al., 2019, Jia et al., 2021b). Although many

104 significant achievements and insights have been made to guide exploration and production,

105 several challenges remain, such as determining exactly how changes in stratigraphy correlate with

106 changes in the mechanical properties of a shale sequence, which can then be used to identify the

107 most suitable intervals for hydraulic fracturing operations (Sethi et al., 2024). Previous studies

108 have attempted to use macroscopic testing to establish the relationship between macroscopic

109 mechanics and sedimentary conditions (Li et al., 2024, Sethi et al., 2024), while they are not able

110   to characterize shale strata continuously and their inability to accurately depict the correlation

111   between shale mechanics and sedimentary condition, especially for the fragile shale samples.

112   Nanoindentation can overcome sampling problems, and a single mechanical test can

113   simultaneously obtain these mechanical parameters. Recent literature mainly discusses the

114   selection of indentation method (Du et al., 2021, Jia et al., 2021a, Shi et al., 2019b, Wang et al.,

115   2022b), fluid influence (Yang et al., 2018, Yang et al., 2016), and component analysis of small

116   sample size for the study of WF-LMX shale mechanics (Long et al., 2021). Few studies

117   concerning the geological effects has been done for the micromechanical properties of shales

118   (Charlton et al., 2023). To the best of our knowledge, there have been no investigations focusing

119   on the microscale mechanical properties, namely elasticity, plasticity, toughness, and brittleness,

120   of the marine shale of the WF-LMX Formation along the southeastern margin of the Sichuan

121   Basin and how these properties are related to sedimentary conditions.

122   In this study, we aim to use nanoindentation technology to perform a thorough mechanical

123   characterization of WF-LMX shales at the microscale and to quantitatively assess the mechanical

124   profile of WF-LMX shales. Specifically, in order to obtain micromechanical parameters, we

125   particularly used a novel method to calculate the shale brittleness index based on nanoindentation

126   data. Additionally, we aim to correlate the measured micromechanical data with the sedimentary

127   conditions (e.g., redox condition and bedding) and rock physics (petromineralogy, reservoir space)

128   of the WF-LMX Formation. This correlation will enable us to identify the controlling factors of

129   shale mechanics at the micro-scale and to investigate how lithofacies influence the

130   micromechanical profile of WF-LMX shales. In general, this mechanical study of WF-LMX

131   shales in the whole layer using nanoindentation technique overcomes the limitations of traditional

132   mechanical testing associated with sample availability. This approach provides a continuous and

133   accurate interpretation profile of mechanical parameters for the design of shale gas development.

134

135   **2 Geological setting and sampling shale samples**

136   The Sichuan Basin and surrounding regions were characterized as stagnant basins during the

137   Late Ordovician to Early Silurian, resulting in the formation of extensive low-energy and anoxic

138   sedimentary environments (Chen et al., 2014). During this period, two significant global

139   transgressions occurred, which contributed to extensive organic-rich shale intervals within the WF

140   Formation and the bottom part of the LMX Formation (see Figure 1a). The black shale gradually

141   shifted from the central sedimentary region to the source region (as shown in Figure 1a), while the

142   paleoenvironment gradually evolved from deep-water shelf environments to semi-deep-water

143   environments and finally to shallow-water shelf environments (Guo and Zeng 2015).

144
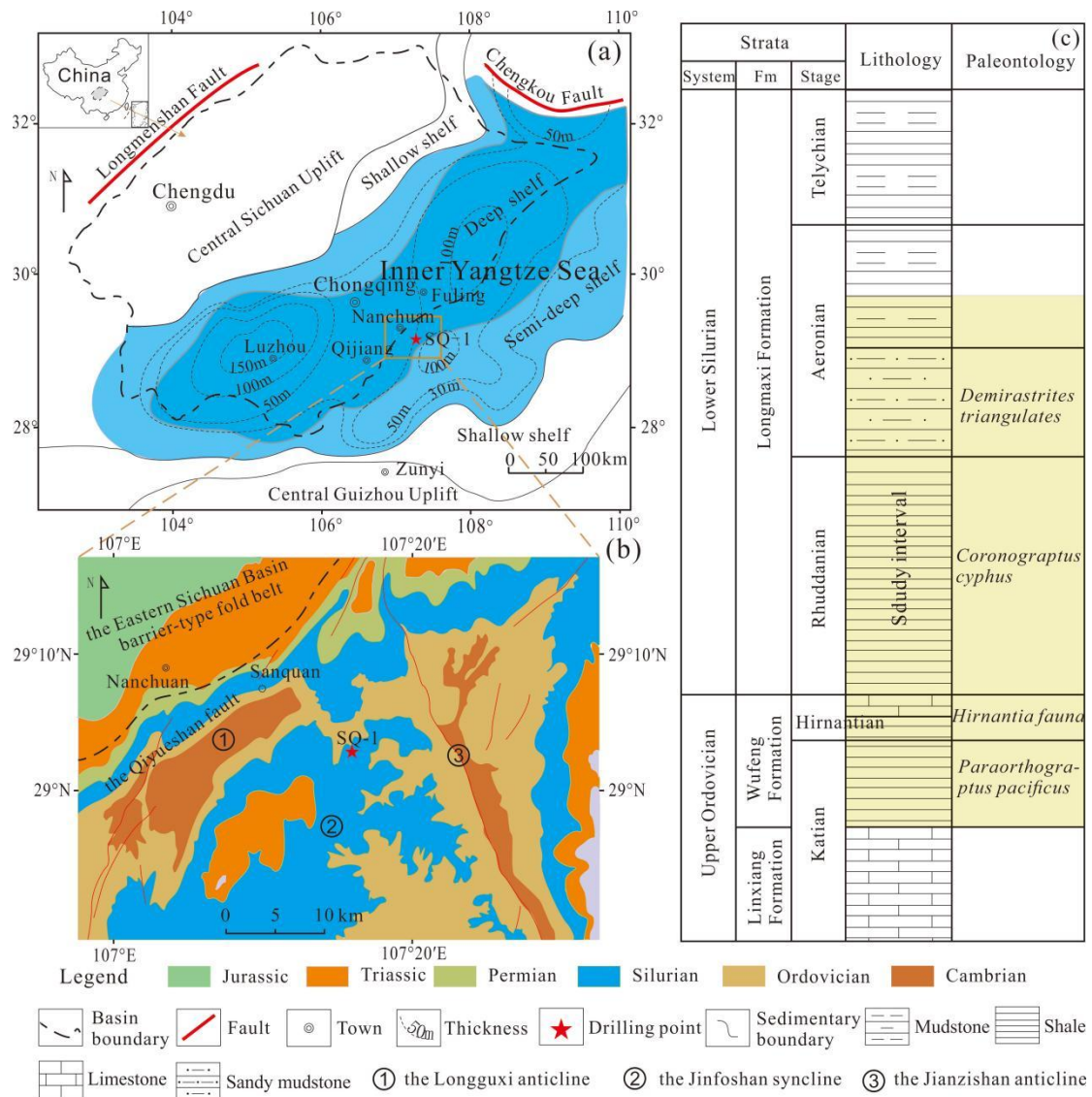
Figure 1. (a) shows a paleogeographic map of the Sichuan Basin and adjacent regions during the Early Silurian. (b) shows the regional, structural, and geological profiles of the Sanquan region, highlighting the exposed strata and the Sanquan-1 well. (c) shows the stratigraphic, lithologic, and paleontologic column, along with the intervals under study (modified from Zheng et al., 2018). Fm = Formation.

The Sanquan-1 (SQ-1) well, located in Sanquan Town, Nanchuan District, Chongqing City, within the Sichuan Basin of China (as shown in Figure 1b), is located on the crest of an anticline

154 and to the east of the Qiyue Shan Fault (see Figure 1b). Core shale samples were collected from

155 the Upper Ordovician Wufeng Formation and the lower part of the Silurian Longmaxi Formation

156 (as shown in Figure 1c). The stratigraphy of the SQ-1 well consists of muddy limestone, siliceous

157 shale, carbonaceous shale, black shale, sandy mudstone and mudstone in sequence from base to

158 top. According to biostratigraphy, petrography and gamma-ray (GR), sequence stratigraphy of

159 Well SQ-1 can be distinguished (Figure 1c). There are two sections in the Longmaxi Formation of

160 the SQ-1 well: the Rhuddanian and Aeronian stages. The Rhuddanian Stage, ranging from 60.5 to

161 84.7 meters in depth, consists of black carbonaceous and black shale. The Aeronian Stage, from 11

162 to 60.5 meters, consists of black shale and grayish-black argillaceous sandstone (Figure 1c). The

163 WF Formation (84.7-90.0 m) contains two parts, the Katian Stage (86.0-90.0 m) and the

164 Hernantian Stage (84.7-86.0 m) (Zheng et al., 2018).

165

166 **3 Samples and method**

167 **3.1. Shale rock samples**

168   Shale core samples were systematically collected from the WF-LMX Formation within the

169 wellbore at intervals of one to one and one-half meters from the bottom up. A total of 27 core

170 samples were collected for analysis. These samples have been used in previous geological and

171 petrological studies targeting for shale gas exploration in WF-LMX shales (Yang et al., 2020,

172 Zheng et al., 2018, 2022). Most of the information regarding total organic carbon (TOC)

173 assessment, mineral composition analysis, major element analysis, experimental assessment of

174 total porosity by mercury injection capillary pressure (MICP), and characterization of nanopore

175 structures by N_2/CO_2 gas adsorption techniques is provided in our previous research (Zheng et al.,

176   2018), and the related data can be found in Tables S1-S2. It is noted that previous studies of these

177   samples have focused primarily on the organic geochemical properties, mineralogy, and porosity

178   of the WF-LMX shale Formation. In contrast, our research primarily investigates the coupling

179   relationship between the micromechanical properties and the sedimentary environment of these

180   shales.

181

182   **3.2 Sample preparation**

183   Shale samples were prepared with cuttings for nanoindentation test, generally 1-10 mm thick

184   (Figure 2a). We chose shale samples oriented perpendicular to the bedding plane (designated X1)

185   and those oriented parallel to the bedding plane (designated X3) (Figure 2b), first cut them into ~5

186   mm thick chips, then impregnated them and cemented them with resin, and ground and polished it

187   using silicon carbide abrasive papers of various mesh sizes ranging from 50 to 2000 grit. This was

188   followed by the application of diamond suspension fluid with particle diameters of 9, 3, and 1

189   micrometer for detailed polishing (Yang et al., 2020). Finally, an IM4000 argon ion mill was used

190   for an additional 1-2 hours of polishing to achieve a very smooth surface. The average roughness

191   (measured as root mean square roughness, Rq) of the shale surface, which measures $30 \times 30 \ \mu m^2$

192   and was measured using atomic force microscopy, is less than 100 nm (Wang et al., 2022b).

193   Figure 2c shows a typical optical microscopy image of the shale sample after grid

194   nanoindentation.

195

3.3 Optical microscopy

The mineralogy was examined using an Olympus 4500P optical microscope under reflected light, which was integrated with the nanoindentation system. This high-resolution optical microscope offers magnifications ranging from 200× to 4000×, making it suitable for precise visualization of the surface area prior to nanoindentation testing.

3.4 Scanning Electron Microscope (SEM)-Energy Dispersive Spectroscopy (EDS) imaging

Following the nanoindentation tests, we used a Hitachi S8010 Scanning Electron Microscope (SEM) integrated with Energy Dispersive Spectroscopy (EDS) to examine the indentations formed on the shale surface. Deviating from standard pre-treatment procedures, the specimens were not coated with a gold layer prior to testing to avoid potential damage to the indentation sites and to ensure unobstructed observation of the indentations. The phase distribution diagram based on elemental composition was quantified by EDS analysis.

3.5 Nanoindentation tests

3.5.1 Nanoindentation and theoretical background

Mechanical nanoindentation tests were performed using an Anton Paar TTX NHT[3] nanoindenter with a diamond Berkovich indenter tip with a radius of curvature between 50 and 100 nm (shown in Figure 2a). A high-resolution optical microscope was integrated into the indenter for precision. Loads ranging from 0.1 to 500 mN were applied to the indenter as it contacted and penetrated the sample surface.

Before performing the indentation tests, a standardized fused silicon sample was used to

218 calibrate the shape of the tip. Thanks to the unique reference ring design of the Anton Paar

219 instrument, automatic thermal drift correction was implemented to ensure data stability. Figure 2d

220 shows a schematic representation of the indentation profile, while Figure 2e shows a typical

221 load-displacement curve (*P-h* curve) consisting of three distinct phases: loading, holding and

222 unloading. The loading phase includes both elastic and plastic deformation components, while the

223 unloading phase captures only the elastic deformation-related strain recovery (Cheng et al., 2002,

224 Yang et al., 2020). Consequently, the area under the unloading curve is referred to as the elastic

225 energy (U_e), and the area enclosed by both the loading and unloading curves represents the

226 irreversible energy (U_p). The total energy (U_t) is the sum of U_e and U_p (Cheng et al., 2002). By

227 analyzing the *P-h* curve, the hardness (*H*) and reduced elastic modulus (E_r) of the shale will be

228 derived (Oliver and Pharr 1992, 2004). In this investigation, a Poisson's ratio of 0.3 was assumed

229 for the shale samples to calculate their Young's modulus (*E*) (Li et al., 2018).

230

231
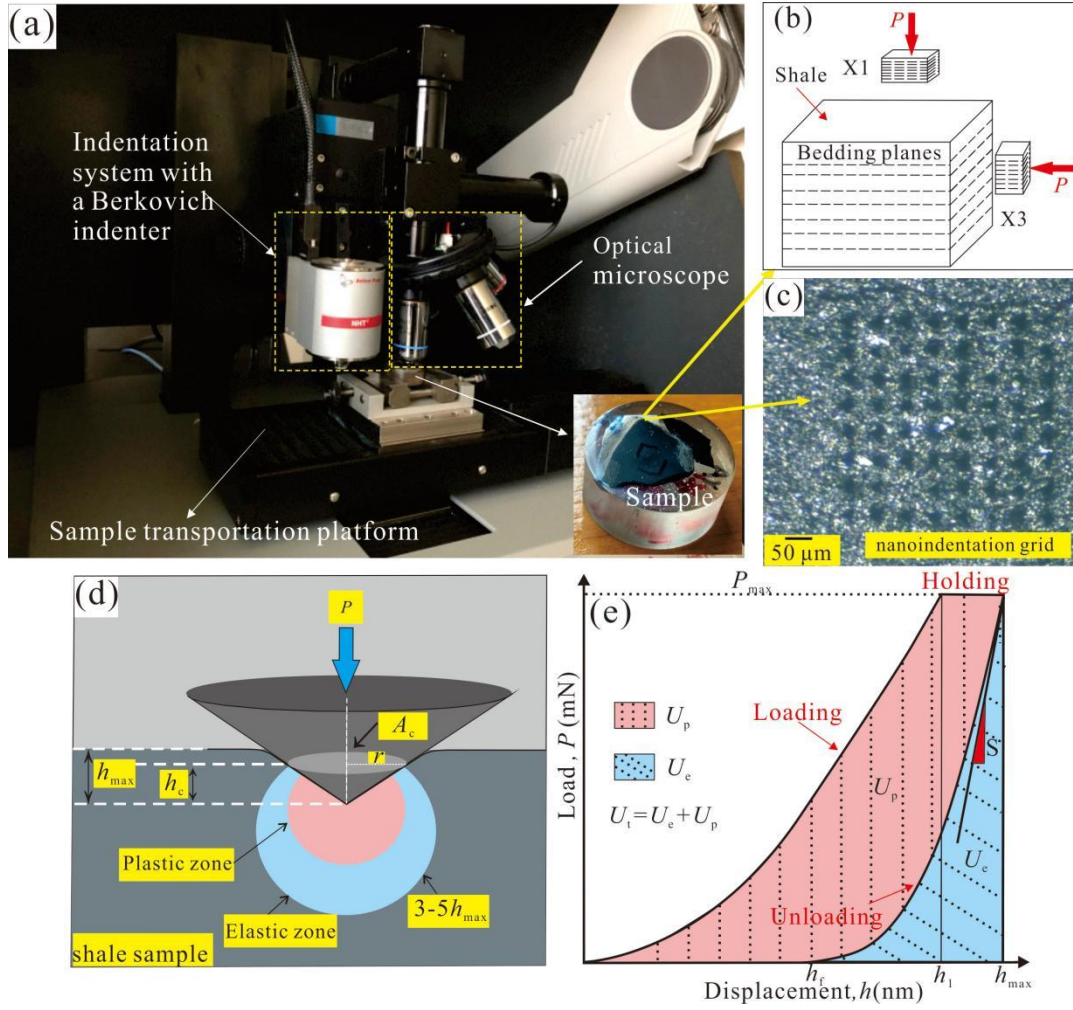
Figure 2. (a) The primary components of the nanoindenter are shown, with the polished specimen

in the lower right corner. (b) shows the specimen with X1 and X3 planes, oriented differently for

nanoindentation testing. (c) shows typical light microscopy images of a shale sample undergoing

nanoindentation. (d) provides a schematic representation of the indentation profile. (e) shows a

typical load-displacement (*P-h*) curve (modified from Wang et al., 2023). Here, *P* is the applied

load, P_{max} is the maximum load, *r* is the contact radius, *S* is the contact stiffness, *h* is the

indentation displacement, while h_f, h_1, and h_{max} are the residual displacement, the displacement at

the onset of the hold phase, and the maximum displacement during nanoindentation, respectively.

The elastic-plastic deformation zone under the indenter is 3-5 times h_{max} (Larsson et al., 1996).

241

3.5.2 Experimental protocols

Constant load holding tests were performed in which the indentation load was applied in a linear fashion until the peak load of 400 mN was reached. Once this peak load was reached, the diamond indenter was held in position for 2 seconds. Finally, the indentation test was completed with a 30-second unloading of the tip. We adopted the statistical nanoindentation method, which is widely used in the mechanical characterization of muti-phase composite materials (Figure 2c). Specifically, the peak load of 400 mN was used (Kumar et al., 2012). Each shale sample surface contained at least 7×7 grid indentations with the distance of at least 60 μm between adjacent indentations (Wang et al., 2022a). Therefore, the size of the indentation areas was approximately 450 μm × 450 μm, which is a much larger representative elementary area (REA) than that proposed by Liu et al. (2018) to ensure an unbiased statistical characterization. Prior to conducting the nanoindentation tests, we first observed the shale surface using a high-resolution optical microscope to determine the representative regions of interest, taking into account the multiscale heterogeneity and mineralogical variability of the shale. we did not find any obvious laminar structure in our shales. The shale surface areas selected for testing exhibited mineralogical characteristics consistent with the overall shale surface.

3.6 Determination of fracture toughness and brittleness index

In this study, the energy-based method was used to calculate the fracture toughness (K_c) of shale (Gautham and Sasmal 2022, Gupta et al., 2020, Liu, 2015, Liu et al., 2016, 2022, Liu 2015, Manjunath and Jha 2019, Zeng et al., 2017, Zeng et al., 2019). After we obtained K_c, the brittleness index (B) based on the mechanical properties can be calculated as (Lawn and Marshall 1979):

265
$$B = \frac{HE}{K_c}$$
(1)

266   The detailled calculation process can be found in the Test S1 of the Supplementary Material.

267

268   **3.7 Statistical Analyses**

269   Statistical significance of the correlations between mechanical parameters and mineralogy,

270   TOC content, porosity and pore volume was determined by SPSS 23.0 software with Pearson

271   correlation analyses and two-tailed Student's tests. This statistical analysis provides a range of

272   correlation coefficients and tests designed to assess the magnitude and direction of the relationship

273   between two variables. This allows us to gain a deeper insight into the patterns and relationships

274   in the data, as well as to uncover potential associations that may go beyond the confines of simple

275   linear correlations. All numerical analyses were performed using Origin 2021, Python 2.0 and

276   Microsoft Excel 2016, and all graphs were made by Origin 2021, Corel Draw X8 and Microsoft

277   Excel 2016.

278

279   **4 Results**

280   **4.1 Mineralogy and indentation of shale**

281   **4.1.1 Optical properties of shale mineralogy**

282   The core samples are mainly composed of quartz and clays (≥70 vol.%) with small

283   percentages of feldspar, carbonate, pyrite and organic matter. Here, we selected two representative

284   samples (i.e., SQ-80b and SQ-90) in terms of their different mineralogical characteristics (i.e.,

285   quartz-rich and clay-rich) to demonstrate the microstructure of the shale. The quartz grains present

286   in the detrital material are translucent and have a grayish white color when viewed under reflected

287 light (Figure 3). They have a variety of irregular shapes characterized by sharp, straight

288 boundaries and are predominantly between 15 and 40 microns in size (Figure 3). It is noteworthy

289 that WF-LMX shales have large amount of authigenic quartz grains, which are usually very small

290 in size, less than 2 μm, and can only be observed by SEM (Milliken et al., 2016, Yang et al., 2020).

291 The clay minerals show dark gray color and are continuously distributed in the shale matrix,

292 constituting the connected skeleton of the shale (Figure 3). Notably, the clays are usually

293 intermixed with nanometer-sized organic matter, forming the organoclay composites (Ma et al.,

294 2015, Yang et al., 2020). Organic matter, consisting mostly of particles smaller than 3 μm, is

295 embedded in matrix voids or intermixed with clay minerals (Figure 3d). Pyrite typically appears as

296 aggregates with dimensions ranging from 1 to 8 μm (Yang et al., 2020). The pyrite and organic

297 matter usually show a grayish white to bright white color under the reflected light. Overall, the

298 quartz-rich shale sample has a coarse-grained texture with large mineral particles such as quartz

299 acting as the supporting skeleton. However, the clay-rich shale has a continuous and fine-grained

300 texture with organoclay composites acting as the framework materials of shale. Notably, the X1

301 plane (as shown in Figures 4a and 4c) exhibits a lower amount of quartz compared to the X3 plane

302 (as shown in Figures 4b and 4d).

303

304
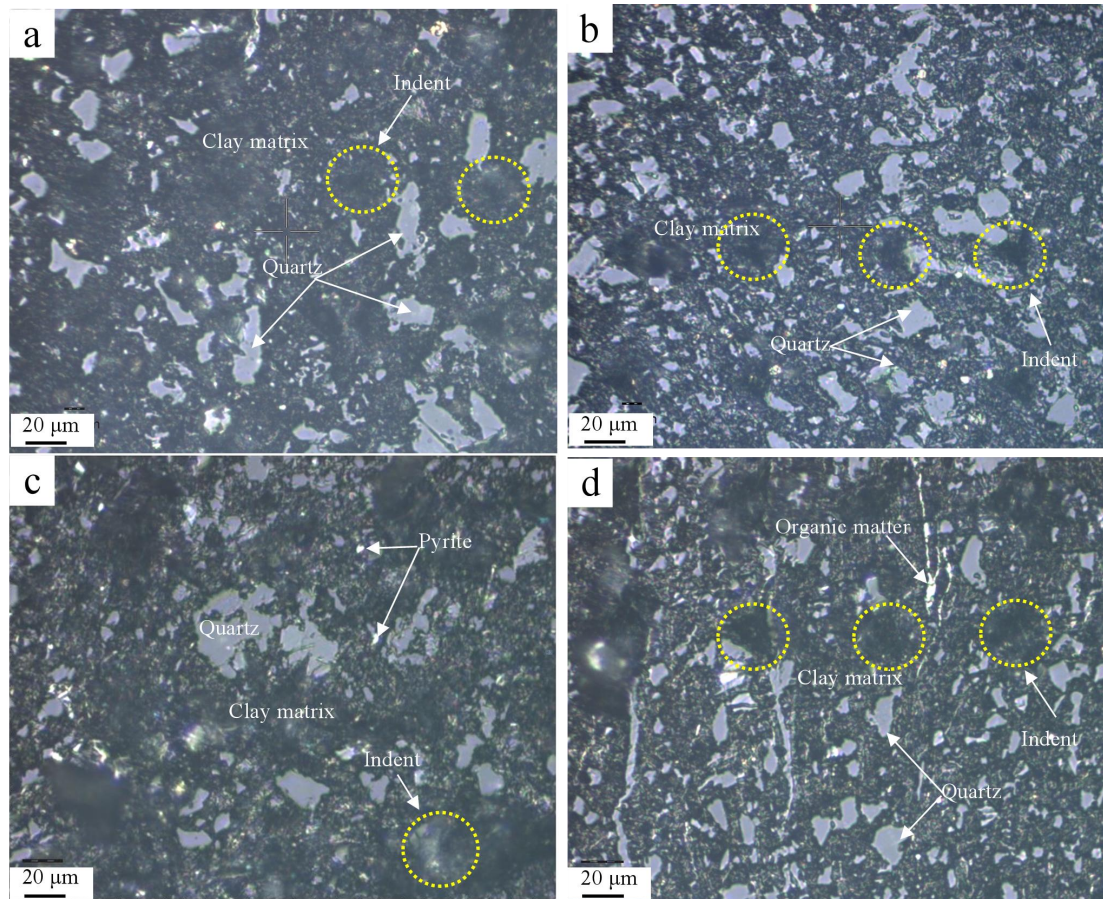
305 Figure 3. Optical microscopy images of the mineralogy of the two representative shale samples.

306 The mineral composition characteristic for (a, b) quartz-rich shale, and (c, d) clay-rich shale. The

307 (a, c) are from X1 plane and (b, d) are from X3 plane. The X1 plane (a, c) of the shale sample has

308 a lower concentration of quartz grains compared to the X3 plane (b, d). The "indent" in (a, b, c and

309 d) represents the indentation residual impressions left in the shale.

310

311 **4.1.2 Nanoindentation of representative microdomains**

312   Figure 4 displays the indents of SQ-78b sample in the X3 plane. Figure 4a shows the

313 panorama of all the indentations. It is observed that some of the indents are located on

314 micro-fractures. Given the strong heterogeneity of the shale, we chose three representative

315 indentation areas for further analysis: the clay-rich area, the organic matter-rich area, and the

316 quartz-rich area. The quartz particle is large, and its surface is very smooth, mainly containing Si

317 and O elements (Figures 4g and 4i). The organic matter in the backscattering diagram appears a

318 black color (Curtis et al., 2012, Zhao et al., 2014), with no fixed form, and is shown in the form of

319 small strips and thin threads (Figure 4f). The clay matrix often combines with the organic matter

320 and mainly contains elements such as Al, Si, C and O (Figures 4e and 4h). The indentation

321 impression in the quartz-rich area measures approximately 20 μm in diameter, while those in the

322 other two areas exceed 30 μm. Microcracks are found around the quartz-rich area, indicating that

323 quartz grain is fractured under the load of 400 mN. In contrast, no significant cracks are observed

324 in the clay-rich and organic matter-rich areas. Furthermore, indentation impressions are clearly

325 visible in the clay-rich and quartz-rich areas. In contrast, no indentation impressions are observed

326 on the surface of the organic matter. This phenomenon has also been found in previous studies

327 (Liu et al., 2019b, Wang et al., 2022c), and is attributed to the high elasticity of organic matter in

328 the high maturity stage.

329
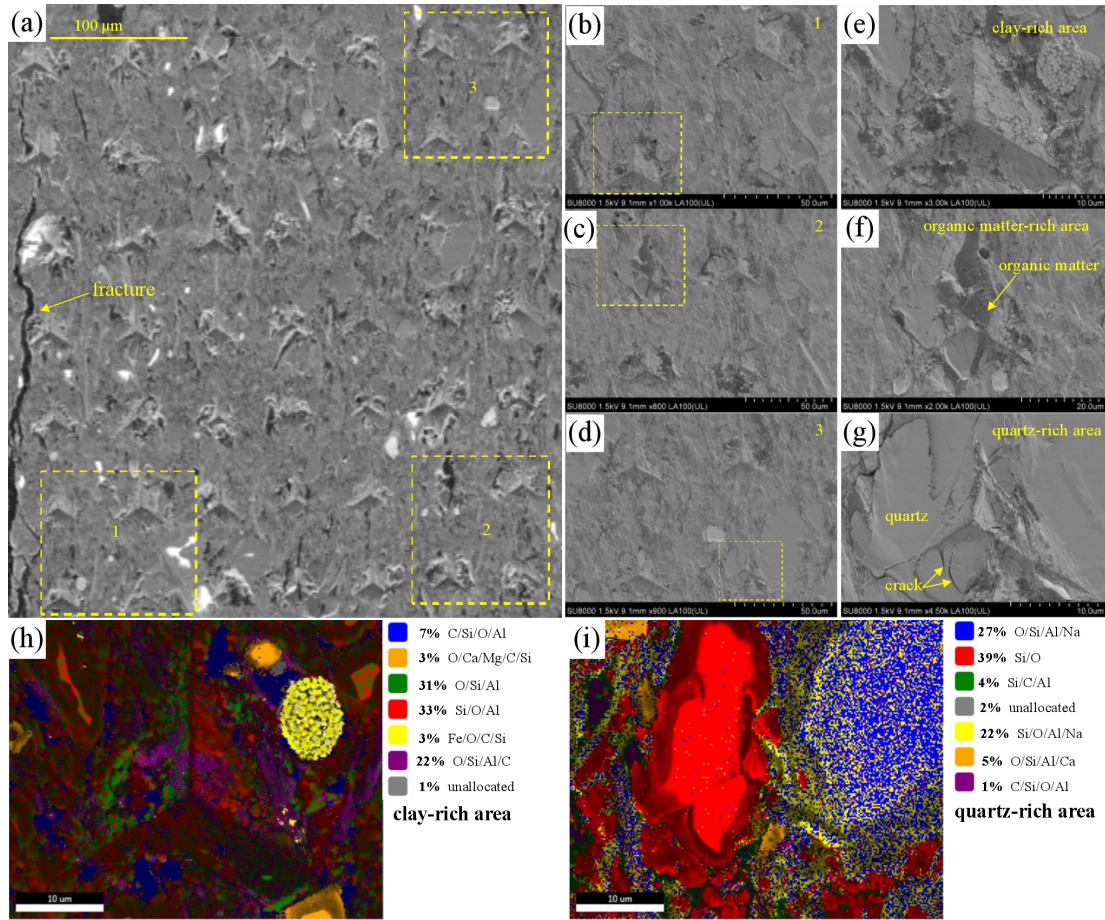
Figure 4. Backscattering (BSE) diagrams (a-g) and phase distribution diagram (h-i) of indented

points in different regions. The numbers 1, 2, and 3 in (b-d) represent the corresponding enlarged

parts. The phase distributions of (h-i) show the indentations are located on the clay-rich area and

quartz-rich area, respectively. The indentation impression in the quartz-rich area has a diameter of

about 20 μm, while the diameters of the other two areas are larger than 30 μm. The indent is

clearly visible in the clay-rich or quartz-rich area, but not in the organic-rich area.

Figure 5 shows the *P-h* curves of all the indents and three typical indents. Figure 5a shows

the maximum displacement ranges from ~3 to 6 μm. The indents present at the fracture zones (as

shown in Figure 4) show significant displacements along with pop-in behavior characterized by

abrupt jumps in displacement. This phenomenon could possibly be due to the development of

341 microcracks during the indentation process. We did not use these data for statistical mechanical

342 analysis. The maximum indentation displacement in the quartz-rich area is significantly smaller

343 than those in the organic-rich area (~4900 nm) and clay-rich area (~4900 nm). The E and H of the

344 indentations in the quartz-rich area are the highest, with values of E=31.7 GPa and H=0.93 GPa,

345 respectively, while those in the organic matter-rich area (E=26.7 GPa, H=0.85 GPa) and the

346 clay-rich area (E=26.3 GPa, H=0.77 GPa) are lower (Table 1). Despite the relatively large

347 differences in elasticoplastic parameters, the fracture toughness of these three indents is relatively

348 similar, ranging from 0.79 MPa·m$^{0.5}$ to 0.85 MPa·m$^{0.5}$. The B value for the indent of quartz-rich

349 area is the highest (43.6 μm^{-1}), followed by the indent in the clay-rich area (34.8 μm^{-1}) and the

350 indent in the organic matter-rich area (29.1 μm^{-1}). Overall, the average mechanical parameters

351 obtained are: E=29.4±3.2 GPa, H=0.95±0.41 GPa, K_c=0.90±0.31 MPa·m$^{0.5}$, and B=37.3±10.5

352 μm^{-1}. Notably, the values of H show a larger variability (43.2% variation) than those of E (10.9 %

353 variation) and K_c (34.4 % variation).

354

355
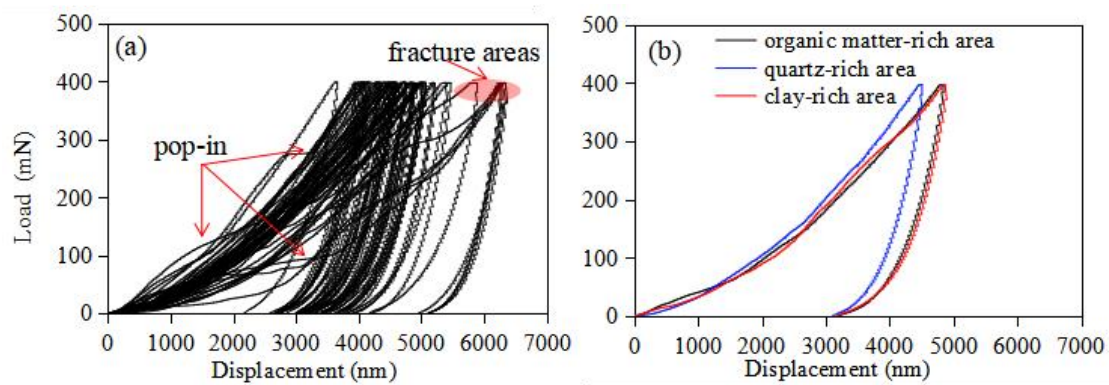
356 Figure 5. Load-displacement curve of (a) all the indentation points, and (b) three typical

357 indentation points in different areas.

358

359 Table 1. Mechanical parameters of indentation points in different regions.

Point	Point of area	E (GPa)	H (GPa)	K_c (MPa·m$^{0.5}$)	B (μm^{-1})
1st	Clay-rich	26.3	0.77	0.79	34.8
13th	Organic matter-rich	26.7	0.85	0.85	29.1
42th	Quartz-rich	31.7	0.93	0.82	43.6
All	All areas	29.4±3.2	0.95±0.41	0.90±0.31	37.3±10.5

4.2 TOC, mineralogy, porosity and major elemental characteristics

Using lithofacies analysis and gamma ray (GR) values, previous researchers have divided the WF Formation into two primary sections from base to top: the Transgressive Systems Tract (TST) and the Highstand Systems Tract (HST), while the LMX Formation was divided into TST, HST and LST (lowstand systems tract) from bottom to top for the SQ-1 well (Zheng et al., 2018) (Figure 6). The TOC content of LMX Formation and WF Formation are in the range of 0.53-3.34 wt.% (average 1.94 wt.%) and 1.30-6.53 (average 3.74 wt.%), respectively. The quartz content values of LMX Formation and WF Formation are in the range of 19.6-43.6 vol.% (average 29.4 vol.%) and 22.7-51.5 vol.% (average 39.3 vol.%), respectively. The clay content values of LMX Formation and WF Formation are in the range of 30.3-54.3 vol.% (average 43.1 vol.%) and 28.8-48.1 vol.% (average 35.5 vol. %), respectively. Feldspar content ranges from 10.6 to 20.4 vol%, with an average of 16.2 vol%. Conversely, the carbonate and pyrite contents are minimal, typically less than 10 vol% (Table S1). The major oxides in the WF-LMX Formations are SiO_2 and Al_2O_3. Other major element concentrations were observed to be <7% (Table S2). The SiO_2 content is the highest of all the oxides in the shale samples, ranging from 58.63% to 76.32%. The average SiO_2 content of WF Formation (69.73%) is higher than that of the LMX Formation (61.54%). The average Al_2O_3 contents in LMX and WF Formations are 13.66% and 8.61%, respectively. The excess SiO_2 contents are in the range of 5.93-58.93% (Table S2).

379   As one moves upward through the drilling profile of the WF-LMX shales, the GR values and

380   TOC content initially increase and then decrease. The quartz content follows a similar pattern to

381   the TOC content, while the clay mineral content shows an opposite trend. Excess silicon is widely

382   distributed in the WF shales (Zheng et al., 2018). Previous research has shown that the excess

383   silicon originates from authigenic silicon in shale, which is closely related to the genesis of

384   siliceous plankton such as diatoms and sponge spicules in sedimentary waters (Schieber et al.,

385   2000). In the SQ-1 well, the excess SiO_2 content varies from low at the bottom, to high in the

386   middle, and then back to low at the top, with the higher values (ranging from 43.04% to 58.93%)

387   being observed in the upper section of the WF Formation. In terms of reservoir space parameters,

388   the total pore volume (V_{total}) and total porosity exhibit ranges of 21.0-41.4 × 10^{-3} cm^3/g and

389   1.3-6.4%, respectively. The higher values are in the WF Formation, where the average values are

390   37.6 × 10^{-3} cm^3/g and 4.5%, respectively. In general, both V_{total} and total porosity are positively

391   correlated with the TOC content (Table S1).

392
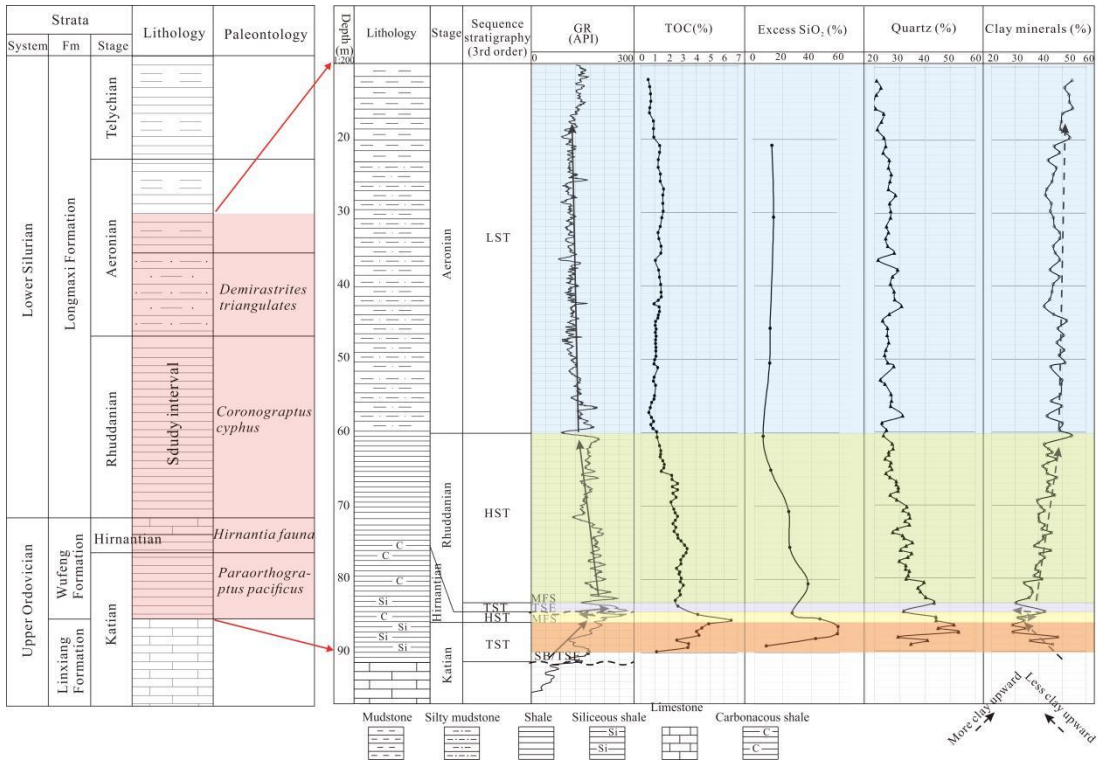
393   Figure 6. A detailed histogram depicting various properties of the WF-LMX shales, including

394   gamma-ray (GR) intensity, TOC content, excess SiO_2 content, quartz content, and clay content

395   (modified from Zheng et al., 2018). HST is the highstand systems tract; LST is the lowstand

396   systems tract; TST is the transgressive systems tract.

397

398   **4.3 Micromechanical profile of WF-LMX shales**

399   Figure 7 shows the longitudinal variations of different micromechanical parameters (E, H, K_c,

400   and B) of WF-LMX Formations in the SQ-1 well. Table S3 presents the corresponding data.

401   Overall, the mechanical parameters in the X1 plane change synchronously with those in the X3

402   plane. Specifically, they first increase and then decrease from the bottom to the top, which is

403   consistent with the variation of quartz and TOC content in the drilling profile. The highest

404   mechanical property values occur in the Hirnantian and the upper Katian of the WF Formation

405   (85-87.6 m), where the contents of TOC (4.2-6.5 wt.%) and quartz (44.4-53.3%) are also very

406   high (Figure 6, Table S4). In fact, the WF Formation was in a deep-water marine shelf setting

407   during the Hirnantian and the upper Katian stages. Conversely, the shales of the upper Aeronian

408   stage of the LMX Formation (SQ-11 and SQ-17), which belong to the shallow-water shelf facies,

409   have the lowest mechanical values.

410   In general, the lower part of the Rhuddanian Stage of the LMX Formation and the Hirnantian

411   and upper Katian stages of the WF Formation have higher values of E, H, and B. Table S4

412   indicates that the average values of micromechanical parameters (E, H, K_c, and B) in the WF

413   Formation are relatively higher than those in the LMX Formation. The micromechanical

414   parameters (E, H, K_c, and B) in the X1 plane are lower than those in the X3 plane.

415
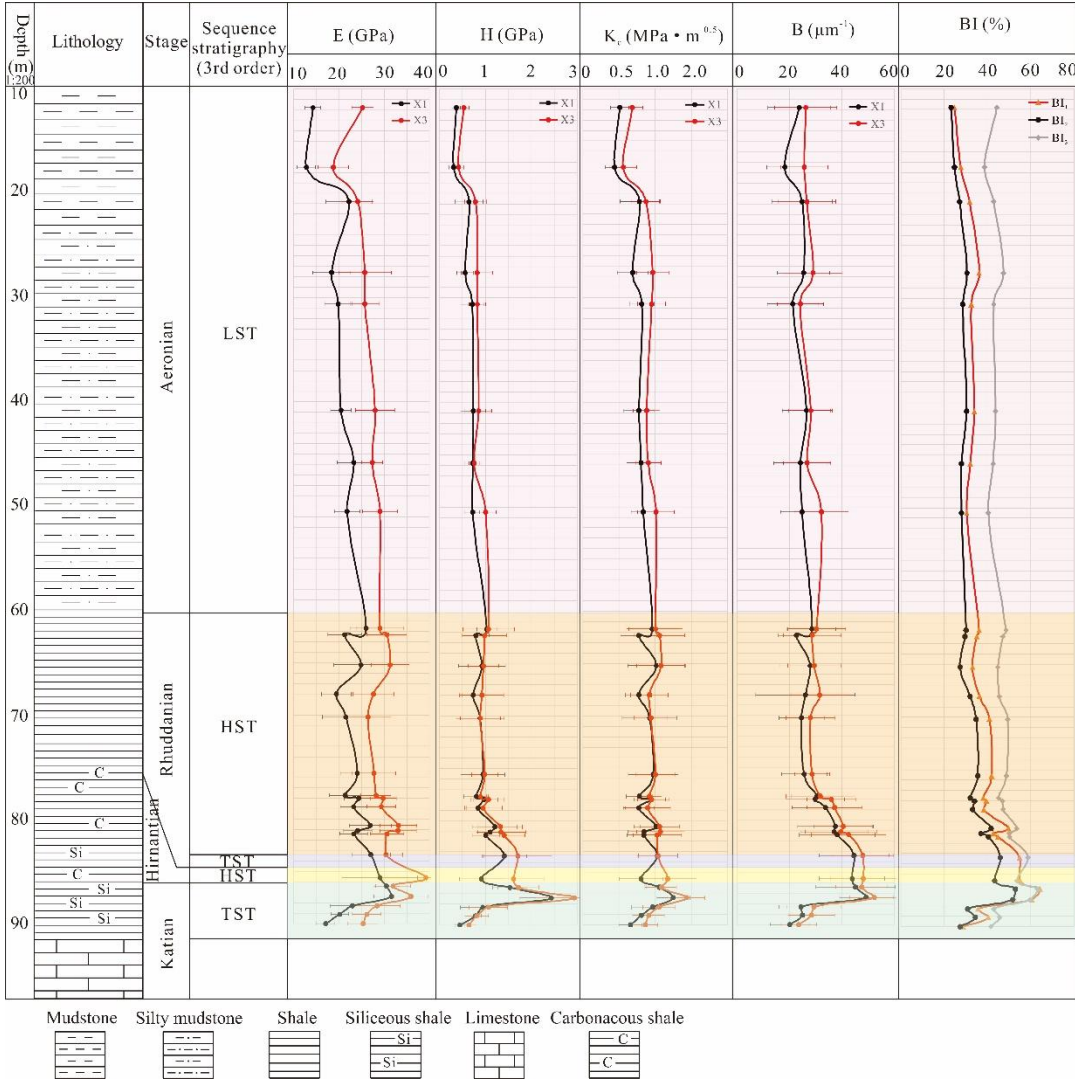
416

417 Figure 7. A histogram of E, H, K_c and BI (brittleness index) of shale in Well SQ-1. X1 indicates a

418 direction perpendicular to the bedding plane of the shale, while X3 indicates a direction parallel to

419 the bedding plane. BI$_1$, BI$_2$, and BI$_3$ are brittleness indices based on mineral composition (as

420 shown in Table 4). From SQ-1 well bottom to the top, E, H, K_c, and BI all show the similar trend,

421 and the bottom of LMX Formation and the upper part of WF Formation (~80-87 m) have large

422 values.

423

424 **5. Discussion**

425 **5.1 Paleo-depositional conditions of WF-LMX shales**

426 **5.1.1 Sedimentary shale site**

427   Al_2O_3 and TiO_2 are commonly used as indicators of terrigenous material, while Mn is

428 considered a marker element from the deep ocean (Adachi et al., 1986, Boynton 1984). The

429 MnO/TiO_2 ratio is generally less than 0.5 in coastal or continental shelf areas and ranges from 0.5

430 to 3.5 in open ocean or deep sea environments (Adachi et al., 1986, Boynton 1984, Sethi et al.,

431 2024). The average MnO/TiO_2 value of 0.06 in the WF-LMX shales indicates a sedimentary

432 environment closer to the continent. The $Al_2O_3/(Al_2O_3+Fe_2O_3)$ ratios in sediments from ridge,

433 basin, and continental margin areas are less than 0.4, in the range of 0.4 to 0.7, and between 0.7

434 and 0.9, respectively (Murray et al., 1991). The $Al_2O_3/(Al_2O_3+Fe_2O_3)$ ratio of WF-LMX shales

435 ranges from 0.65 to 0.78, with an average of 0.71, suggesting a continental margin sedimentary

436 environment. In addition, the K_2O/Na_2O vs. SiO_2 and SiO_2/Al_2O_3 vs. K_2O/Na_2O plots can also be

437 used to determine the ancient and modern tectonic backgrounds of the basins (Roser and Korsch

438 1988, Sethi et al., 2024). In Figure 8a-b, the WF-LMX shales show high SiO_2/Al_2O_3 ratios,

439 K_2O/Na_2O ratios, and SiO_2 values. The majority of the data points are within the passive

440 continental margin. Therefore, the WF-LMX shales in the study area are indicative of a passive

441 continental margin sedimentary environment.
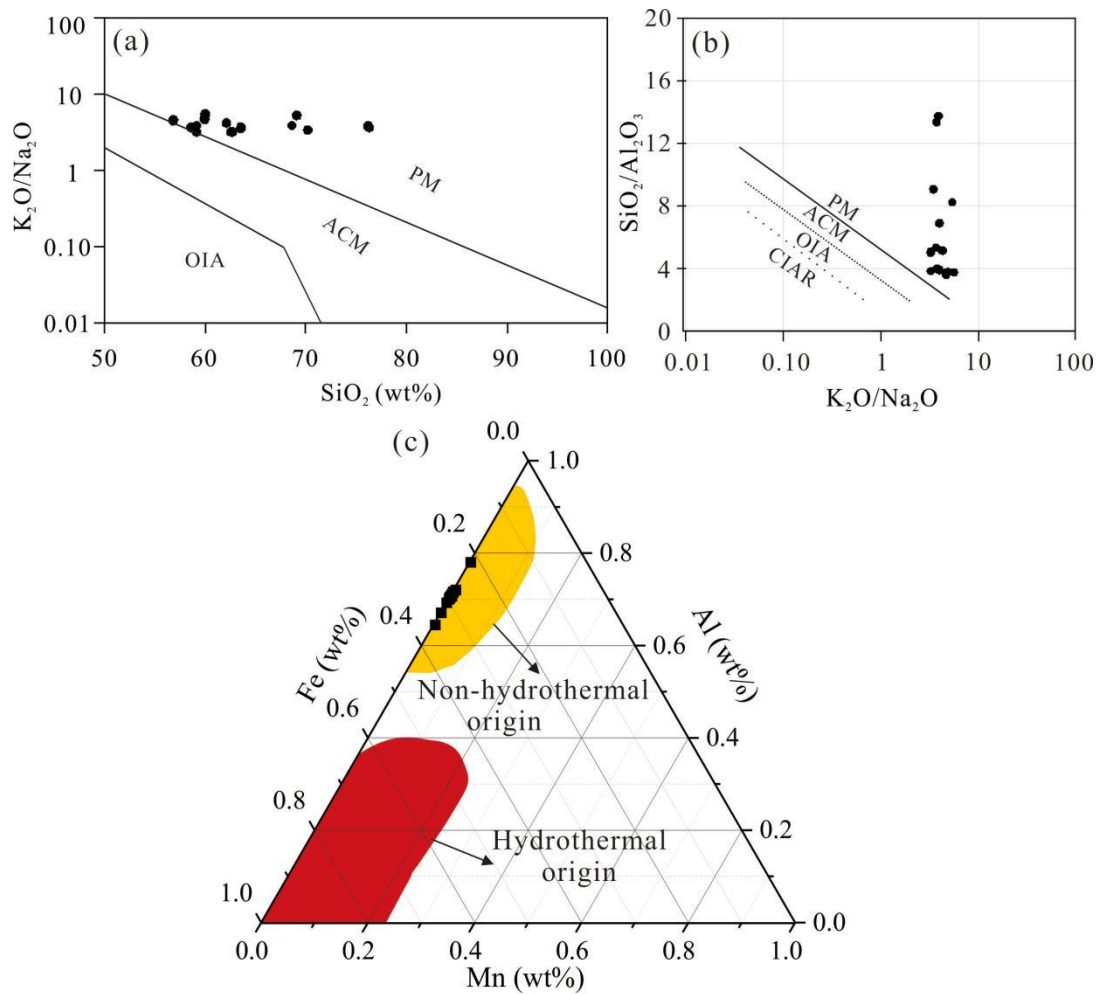
Figure 8. (a) Depositional position classification diagrams (a) (after Roser and Korsch. (1988)) and (b) (after Maynard. (1982)). Identification origin of hydrothermal-biogenic sedimentary (Adachi et al., 1986). PM=passive continental margin; ACM=active continental margin; CIAR=continental island arc; OIA=oceanic island arc.

5.1.2 Sources of silicon

Currently, the main sources of silicon in shales include biogenic, terrestrial detrital, and hydrothermal origins (Adachi et al., 1986, Reynolds and Verhoogen 1953). Al_2O_3 is typically indicative of terrestrial detrital input. When the SiO_2/Al_2O_3 ratio is close to 3, the silicon is primarily of crustal origin. However, when the ratio exceeds 3, silicon is primarily derived from

453 biogenic and hydrothermal processes (Boström et al., 1973). The SiO_2/Al_2O_3 values of the

454 WF-LMX shales range from 3.63 to 13.73 (with an average of 6.42), suggesting that silicon in

455 these shale samples is not primarily derived from terrestrial detrital sources. In particular,

456 geochemical proxies such as (Fe + Mn)/Ti ratios above 25 ($\pm$ 5) and Al/(Al + Fe + Mn) ratios

457 below 0.35 are recognized as the presence of hydrothermal activity during deposition (Boström

458 and Peterson 1969, He et al., 2016). The WF-LMX shale samples exhibit (Fe + Mn)/Ti ratios

459 ranging from 5.8 to 11.3, with an average of 8.9, while the Al/(Al + Fe + Mn) ratios exhibit a

460 narrower range of 0.64 to 0.78, with an average of 0.71 across the data set. This result indicates

461 that silicon in the WF-LMX shale samples is not primarily derived from hydrothermal sources.

462 Furthermore, by observing the Mn-Al-Fe ternary diagram (Figure 8c), all the sample data fall

463 within the non-hydrothermal origin range. It is commonly believed that a SiO_2/Al_2O_3 ratio

464 exceeding 3.0 typically suggests a primarily biological origin (Boström et al., 1973). In the case of

465 the WF-LMX shale samples, the SiO_2/Al_2O_3 values varied between 3.63 and 13.34, with an

466 average of 6.42. This indicates that the silica source in these shale samples was predominantly

467 influenced by biogenic input.

468

469 **5.1.3 Paleoclimate and chemical weathering**

470 Cox (1995) proposed the Index of Component Variation (ICV), which is calculated as the

471 molar ratio of (Fe$_2$O$_3$+ K$_2$O + Na$_2$O + CaO* + MgO +MnO+TiO2), to Al$_2$O$_3$. According to Cullers

472 et al. (2000), an ICV greater than 1 in fine-grained clastic rocks suggests low clay content and

473 originally deposition in a tectonically active area. Conversely, an ICV less than 1 indicates high

474 clay content resulting from chemical weathering or redeposition. In this study, the ICV values of

475 the samples (1.18-1.46, see Table S2) exceed 1, which confirms the first deposition without

476 redeposition and can reflect the weathering degree and paleoclimate of the source area.

477   The process of chemical weathering typically results in the depletion of elements such as Ca,

478 Na, and K, while promoting the relative accumulation of Al and Ti (Fedo et al., 1995, Nesbitt and

479 Wilson 1992). To quantify the extent of chemical weathering in sediment source areas, previous

480 researches have established indices such as the chemical index of alteration (CIA = $100 \times Al_2O_3$ /

481 $(Al_2O_3 + CaO^* + Na_2O + K_2O)$) (Nesbitt and Wilson 1992, Nesbitt and Young 1982) and

482 plagioclase index of alteration (PIA) (PIA = $100 \times (Al_2O_3 - K_2O)$ / $((Al_2O_3 - K_2O) + CaO^* +$

483 Na_2O)) (Fedo et al., 1995). The units of the oxides used in these calculations are molar masses.

484 CaO^* refers specifically to the CaO content in silicate minerals. Since the CaO content in silicate

485 minerals is often comparable to that of Na_2O, a correction method is applied: if the molar amount

486 of CaO is greater than that of Na_2O, CaO = Na_2O; conversely, if the molar amount of CaO is less

487 than that of Na_2O, no correction for CaO is required. The sample trend is generally parallel to the

488 A-CN edge (Figure 9), indicating that potassium (K) has not been significantly leached during

489 weathering and may be weakly affected by potassium metasomatism. In general, CIA values

490 between 50-60 and PIA between 50-69 correspond to low weathering intensity, while CIA

491 between 60-80 and PIA between 69-86 indicate moderate weathering, and CIA between 80-100

492 with PIA between 86-100 represent intense weathering conditions (Li et al., 2024, Nesbitt and

493 Young 1982, Reimann and de Caritat 2012). For the WF-LMX shale samples, the calculated CIA

494 indices range from 64.2 to 70.2 (mean = 65.9) (Figure 9; Table S2), and the PIA values range from

495 72.8 to 82.8 (mean = 76.94). These results indicate that the source rocks have experienced a

496 consistent stable and moderate intensity of chemical weathering. In addition, the CIA index is

497   commonly used to evaluate paleoclimatic conditions (Fedo et al., 1995, Nesbitt and Wilson 1992).

498   In hot, humid paleoclimates, CIA indexes fluctuate between 80 and 100, while warm, humid

499   environments show values between 60 and 80. Conversely, cold, arid paleoclimates generally

500   record CIA values in the range of 50 to 60 (Nesbitt and Wilson 1992). CIA values decrease from

501   the lower to middle-upper part of the Wufeng Formation and then remain relatively stable at

502   higher values in the Longmaxi Formation. This suggests that the paleoclimate shifted from warm

503   and humid to cold and arid before returning to warm and humid conditions. However, the average

504   CIA value of the WF-LMX Formation is 65.9, which generally indicates deposition under warm,

505   humid conditions. It should be noted that this interpretation is based solely on major element data.

506   To   more   precisely   determine   the   paleoclimatic   conditions,   further   validation   through

507   carbon-oxygen isotopes and palynological fossils is necessary.

508
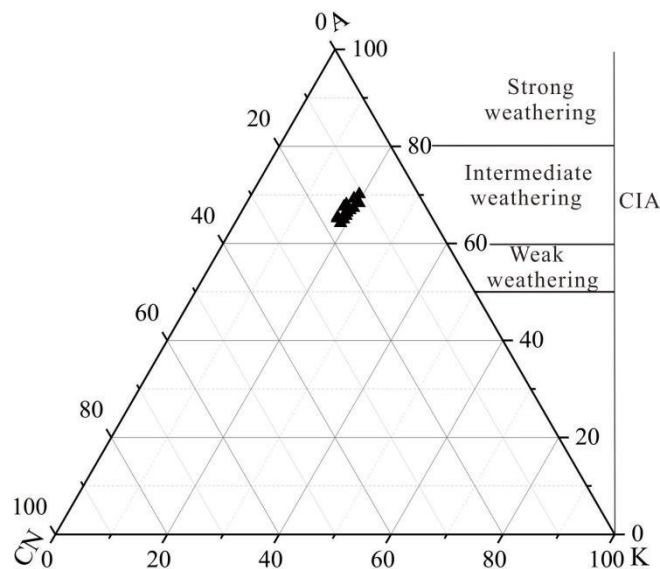
509   Figure 9. Temary plots of Al_2O_3 -(CaO^* + Na_2O)-K_2O (A-CN-K) in molar proportions that

510   reflecting the intensity of weathering (based map from (Nesbitt and Young 1982)). Here CaO^*

511   denotes the CaO content specifically within the silicate component.

512

5.1.4 Redox conditions

Previous studies have found that the redox indicators (e.g., U/Th, Ni/Co, and Mo values) of the WF-LMX shales are positively correlated with TOC content (Li et al., 2017, Yan et al., 2018, Wang et al., 2024, Wei et al., 2021). Based on the TOC content column profile of the SQ-1 well (Figure 6), it can be inferred that the bottom of the LMX Formation and the upper-middle part of the WF Formation had the strongest reducing conditions, with TOC content exceeding 2.5% formed in anoxic environments, while shale sections with TOC less than 2% were mainly formed in oxic environments (Li et al., 2017). Furthermore, the high excess silicon content in organic-rich shales in the middle-upper part of the WF Formation and the bottom of the LMX Formation indicates relatively high paleoceanic productivity during deposition, which is consistent with previous findings (Li et al., 2017, Yan et al., 2018).

5.2 Effect of components on micromechanical properties

5.2.1 Young's modulus, hardness, and fracture toughness

The sedimentary environment controls the mineral composition, TOC content, and pore characteristics of organic-rich shales. Here we discuss the effect of constituents on the mechanical properties of WF-LMX shales. For both X1 and X3 planes, the linear positive correlation between Young's modulus of shale and the quartz content is good (Figure 10a). The reason is that quartz is thought to be a brittle mineral. The measured Young's modulus of bulk shale is enhanced by elevated concentrations of the quartz. In particular, Young's modulus of shale on both X1 and X3 planes and the content of excess SiO_2 show a positive correlation, especially for that on the X1 plane (Figure 10i). This means authigenic quartz plays an important role in increasing the strength

535 of shale and improving the fracturability of the shale. Conversely, Young's modulus and clay

536 mineral content show a negative correlation in different planes (Figure 10b). As clay minerals

537 inherently act as plastic components within shale matrices. While increased clay content decreases

538 mechanical properties of shale, the scientific consensus remains unresolved regarding the brittle

539 classification of feldspar, calcite, dolomite, and pyrite (Glorioso and Rattia 2012, Wang and Gale

540 2009). As shown in Figures 10c-10f, there is no direct positive relationship between the content of

541 these minerals and Young's modulus values. Notably, there is a negative correlation between

542 calcite content and modulus measurements (Table 2, Figure 10c), which is consistent with

543 previous triaxial compression studies of core samples (Diao 2013). This phenomenon may be due

544 to two factors: (1) relatively low calcite volume fractions (vol.% < 8%), and (2) isolated grain

545 distribution patterns within the shale matrix. Such dispersed rigid particles (calcite, dolomite, and

546 pyrite) fail to form effective load-bearing frameworks, thereby precluding embrittlement

547 enhancement by mineral reinforcement.

548 Compared to inorganic minerals, organic matter has lower density (approximately half the

549 density of the shale rock minerals), and much lower modulus values in the range of 1-20 GPa

550 (Fender et al., 2020, Wang et al., 2024). However, Young's modulus is statistically positively

551 correlated with TOC content of WF-LMX shales in both planes (Figure 10g). The reason is that

552 the contents of quartz and organic matter show a synchronous and co-directional trend in the

553 stratigraphic profile. While organic matter inherently reduces shale strength, quartz emerges as the

554 primary determinant in increasing shale Young's modulus, thereby leading to a consistent

555 contribution relationship between organic matter and the Young's modulus of shale. Young's

556 modulus shows no correlation with total nanopore volume or the total nanopore surface areas

557 (Figure 10k-10l), and even a weak positive correlation with porosity (measured by MICP method)

558 (Figure 10j). The main reason is that in the WF-LMX shale, high porosity and total pore volume

559 are associated with high organic content (Table 2), which is positively correlated with the content

560 of authigenic quartz. The influence of pores on shale mechanical properties may be compensated

561 by authigenic quartz. On the other hand, the relationship between Young's modulus and individual

562 components shows a more pronounced correlation in the X1 plane compared to the X3 plane, a

563 disparity that could be primarily due to the preferential orientation of mineral particles during

564 sedimentation and the distinct mechanical behaviors inherent to their depositional environments.

565

566
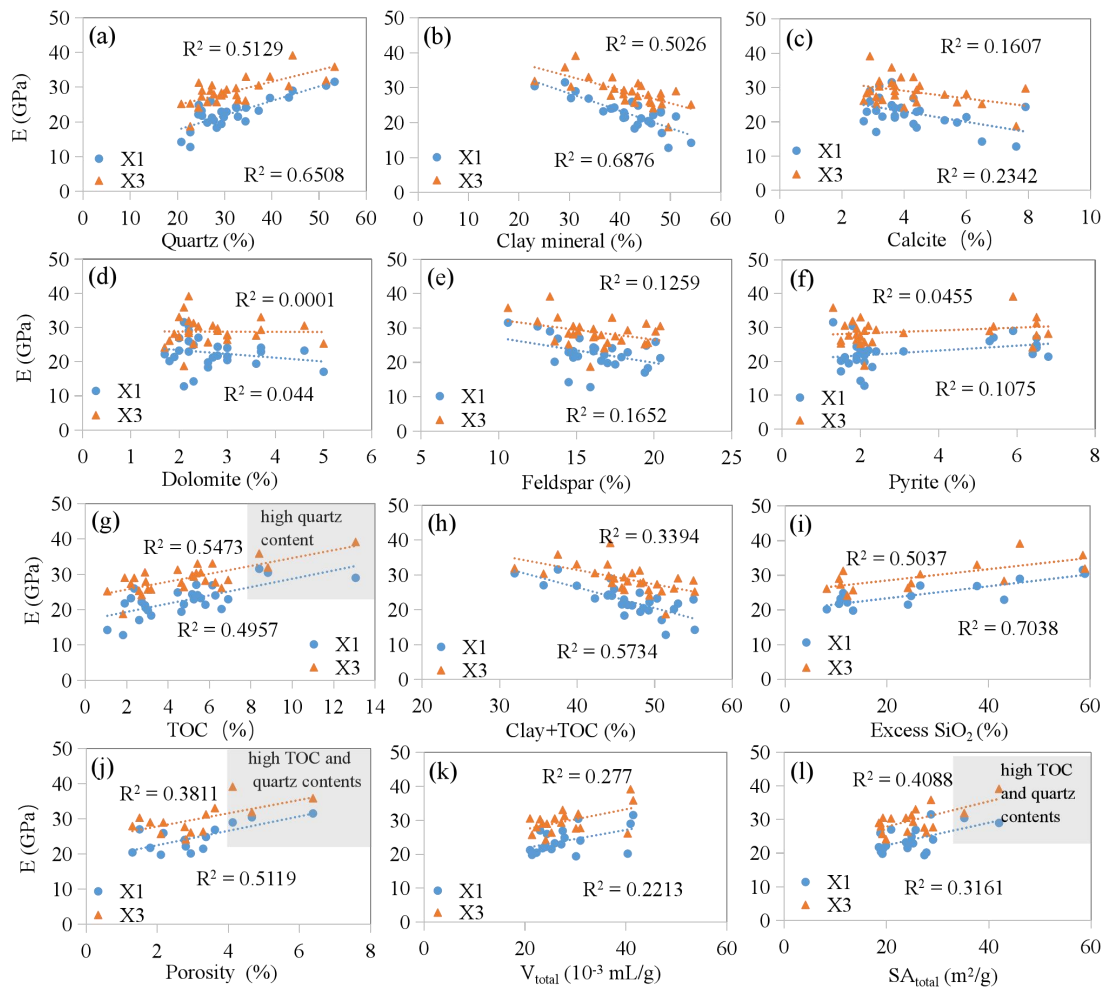
567 Figure 10. Correlation of shale Young's modulus (E) with volumetric proportions of matrix

568   constituents (a-h), excess SiO_2 content (i), porosity (j), total nanopore volume (k), and surface

569   areas (l). Note:Q=Quartz, F=Feldspar, Car=Carbonate, Dol=Dolmite, Py=Pyrite, V_{total}=the total

570   nanopore volume, SA_{total}=the total nanopore surface areas. The percentage of various components

571   is the volume percentage. The marked three samples in (g and j) are in high quartz, TOC contents

572   and porosity. Young's modulus shows high dependence on quartz, clay, and clay +TOC content,

573   especially along the X1 plane, while it has weak or no correlation with the change in the content

574   of other rock constituents, including the carbonates, organics and pores.

575

576   Figure 11 shows a good positive linear relationship between Young's modulus and both

577   hardness and fracture toughness. The relationship between Young's modulus and hardness exhibits

578   greater strength along the X1 plane (R^2=0.74) compared to the X3 plane (R^2=0.60). Conversely,

579   the correlation between Young's modulus and fracture toughness maintains comparable

580   magnitudes in both the X1 and X3 planes (Figure 11). Generally, the influence of components on

581   hardness or fracture toughness is equivalent to that of Young's modulus. This observation may be

582   due to the fact that Young's modulus serves as a direct measure of material stiffness, with higher

583   values corresponding to increased resistance to deformation and crack propagation, thereby

584   contributing to higher fracture toughness values (Gupta et al., 2020).

585
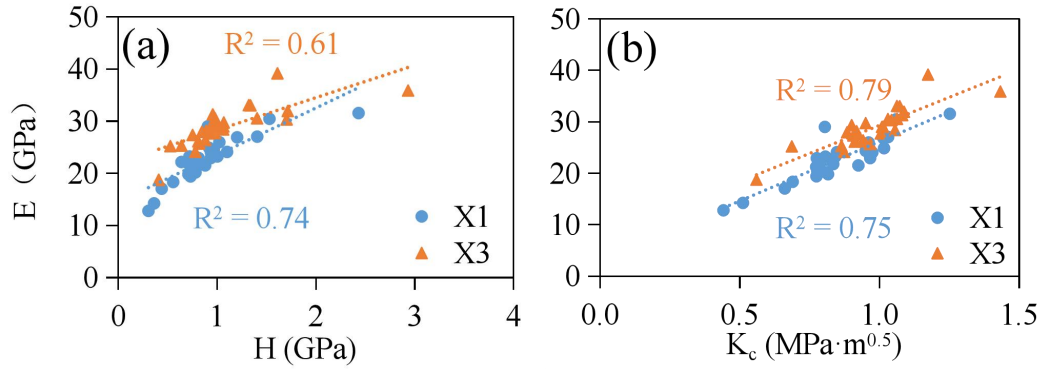
Figure 11. Relationships between E and (a) H, or (b) Kc.

Table 2 presents the statistical correlation analysis between the mechanical parameters and the mineralogical compositions, TOC content (volumetric fraction), porosity, and total pore volume for the shale samples via SPSS software. Similar to the linear fit results observed in Figure 10, the micromechanical properties (E, H, and K_c) of the WF-LMX shale show a good positive linear relationship with quartz, Q+Dol (quartz and dolomite), and QFC (quartz, feldspar, and carbonate) mineral assemblages, while exhibiting a negative correlation with clay mineral abundance and O/C (clay+TOC) composite content. Taken together, these relationships suggest that the micromechanical behavior of the shale is predominantly controlled by the proportional content of quartz, clay minerals, and organic-clay complexes, as these components form the primary structural framework of the shale matrix and collectively determine the overall mechanical performance of the WF-LMX Formation.

Table 2. Correlation matrix to investigate the dependence of mechanical parameters on mineralogy, TOC content (volume fraction), porosity and pore volume.

	TOC	Qtz	Clay	F	Cal	Dol	Py	O/C	Q+Dol	QFC	ϕ	PV$_{total}$	E1	E3	H1	H3	Kc1	Kc3	B1	B3
TOC	1.00																			
Qtz	0.82	1.00																		
Clay	-0.79	-0.93	1.00																	
F	-0.57	-0.66	0.43	1.00																
Cal	-0.32	-0.31	0.26	-0.02	1.00															
Dol	-0.12	-0.12	0.05	0.37	-0.02	1.00														
Py	0.24	0.05	-0.23	0.00	-0.13	-0.38	1.00													
O/C	-0.57	-0.85	0.95	0.31	0.19	0.01	-0.18	1.00												
Q+Dol	0.82	1.00	-0.93	-0.63	-0.32	-0.03	0.01	-0.85	1.00											
QFC	0.60	0.77	-0.88	-0.07	-0.22	0.25	-0.02	-0.88	0.80	1.00										
ϕ	0.72	0.56	-0.58	-0.40	-0.41	-0.39	0.16	-0.39	0.55	0.43	1.00									
PV$_{total}$	0.81	0.60	-0.43	-0.66	-0.43	-0.28	-0.03	-0.16	0.58	0.24	0.59	1.00								
E1	**0.70**	**0.81**	**-0.83**	-0.41	-0.48	-0.21	0.33	**-0.77**	**0.79**	**0.65**	0.50	0.47	1.00							
E3	**0.75**	**0.72**	**-0.71**	-0.36	-0.40	-0.01	0.21	-0.58	**0.72**	**0.62**	0.37	0.50	0.84	1.00						
H1	0.57	**0.86**	**-0.79**	-0.53	-0.33	-0.17	0.05	**-0.78**	**0.85**	**0.67**	0.40	0.45	0.85	0.69	1.00					
H3	**0.66**	**0.89**	**-0.80**	-0.57	-0.33	-0.09	0.03	**-0.75**	**0.89**	**0.69**	0.32	0.52	0.83	0.78	0.96	1.00				
Kc1	0.50	**0.69**	**-0.68**	-0.32	-0.46	-0.18	0.24	**-0.67**	**0.68**	0.57	0.55	0.32	0.89	0.65	0.88	0.77	1.00			
Kc3	**0.63**	**0.73**	**-0.68**	-0.31	-0.54	-0.06	0.14	**-0.60**	**0.72**	**0.62**	0.44	0.53	0.86	0.86	0.84	0.87	0.84	1.00		
B1	**0.75**	**0.91**	**-0.90**	-0.57	-0.26	-0.06	0.18	**-0.84**	**0.91**	**0.74**	0.42	0.47	**0.83**	**0.81**	**0.82**	**0.89**	**0.64**	**0.89**	1.00	
B3	**0.75**	**0.91**	**-0.88**	-0.59	-0.21	-0.03	0.10	**-0.81**	**0.92**	**0.74**	**0.62**	0.47	**0.80**	**0.80**	**0.81**	**0.89**	**0.60**	**0.70**	**0.98**	1.00

Note: Qtz = quartz, F = feldspar, Cal = calcite, Dol = dolomite, Py = pyrite O/C = clay + TOC, QFC = total volume content of quartz, feldspar, and carbonate minerals, ϕ = porosity, PV$_{total}$ = total nanopore volume, Superscripts 1 and 3 after mechanical parameters denote measurements along the parallel bedding plane (X1) and perpendicular bedding plane (X3), respectively. $R^2 > 0.6$ are shown in bold. Negative signs (e.g. "-0.90") indicate inverse correlations between parameters. The micromechanical parameters (E, H, Kc, and B) show strong dependencies on quartz abundance, clay content, O/C ratio, Q+Dol assemblage, and QFC mineral fractions, with nearly all correlation coefficients exceeding 0.60. This underscores their dominant control over the mechanical behavior of the shale.

599

5.2.2 Brittleness index

Table 2 shows that the B value based on micromechanical properties is strongly positively correlated with quartz (R^2=0.91), Q+Dol ($R^2 \geq 0.91$) and QFC (R^2=0.74) contents, and negatively correlated with clay ($R^2 \geq 0.88$), and clay+TOC contents ($R^2 \geq 0.81$). However, no significant correlations were observed between these parameters and other individual minerals, porosity, or total nanopore volume. Notably, the R^2 values for the correlations between the brittleness index (B) and mineralogical constituents were similar to those for Young's modulus (E) and hardness (H), but had consistently higher magnitudes (Table 2). Therefore, quartz, especially for the authigenic quartz, as a distinct constituent of marine shale, plays an important role in enhancing the brittleness of shale. The B is strongly positively correlated with the E and H in both the planes, indirectly suggesting that the effect of component on B in shale is similar to that of E and H. To explain the accuracy of the brittleness index calculated based on micromechanical properties, mineral composition method and micromechanical properties based on nanoindentation method are compared to characterize the brittleness of shale. Due to the disunity of brittle minerals, three typical formulas based on mineral composition are each selected. Table 3 shows the brittle mineral and the corresponding formulas.

Table 3. Brittleness index model based on mineral composition (V=volume fraction).

Model	Equation	Brittle minerals	Reference
1	$BI_1=V_{Qtz}/(V_{Qtz}+V_{carb}+V_{clay})$	Quartz	Jarvie et al. (2007)
2	$BI_2=(V_{Qtz}+V_{Dol})/(V_{Qtz}+V_{carb}+V_{clay+TOC})$	Quartz and dolomite	Wang and Gale (2009)
3	$BI_3=(V_{Qtz}+V_{cab})/(V_{Qtz}+V_{carb}+V_{clay+TOC})$	Quartz and carbonate	Glorioso and Rattia (2012)

Figure 12 shows that the brittleness index has a better linear positive correlation with E along

620   the X1 plane than along the X3 plane. The correlations between BI_1 and E are the strongest among

621   the brittleness indices (BI_1, BI_2, and BI_3) along both the X1 (R^2=0.70) and X3 planes (R^2=0.49).

622   The correlation between the brittleness index (BI_1, BI_2, and BI_3) and H in the X1 plane is close to

623   that in the X3 plane. The correlations between the brittleness index (BI_1, BI_2, and BI_3) and H are

624   almost all larger than those between E and the brittleness indices. This suggests that H in the X3

625   plane is more sensitive to the brittleness index than E. The reason may be related to the presence

626   of various mineral phases and their overall physical properties. E is an inherent property of a

627   material, fundamentally related to atomic bonds, while H measures the resistance to local plastic

628   deformation caused by mechanical indentation or wear, which mainly depends on the

629   microstructure or the arrangement of molecules and atoms (Liu et al., 2021). This difference may

630   lead to the varying correlations with the brittleness index. The B value, determined from the

631   micromechanical properties calculated from nanoindentation, exhibits a strong correlation with the

632   mineral component-based BI_1, BI_2, and BI_3 values (Figures 12g-i). Moreover, it shows a similar

633   trend of changes, from the base to the top of the SQ-1 well, as the BI_1, BI_2, and BI_3 values,

634   indicating a high brittleness index at the lower interval of the LMX Formation and the upper

635   interval of the WF Formation, between ~80.0-87.0 m (Figure 7). Compared with Young's modulus

636   from conventional logging, we can obtain not only the Young's modulus of shale via drill cuttings,

637   but also predict its brittleness in the X1 and X3 planes (Figure 7). Therefore, nanoindentation

638   technology shows great potential for predicting the brittleness index of shale.
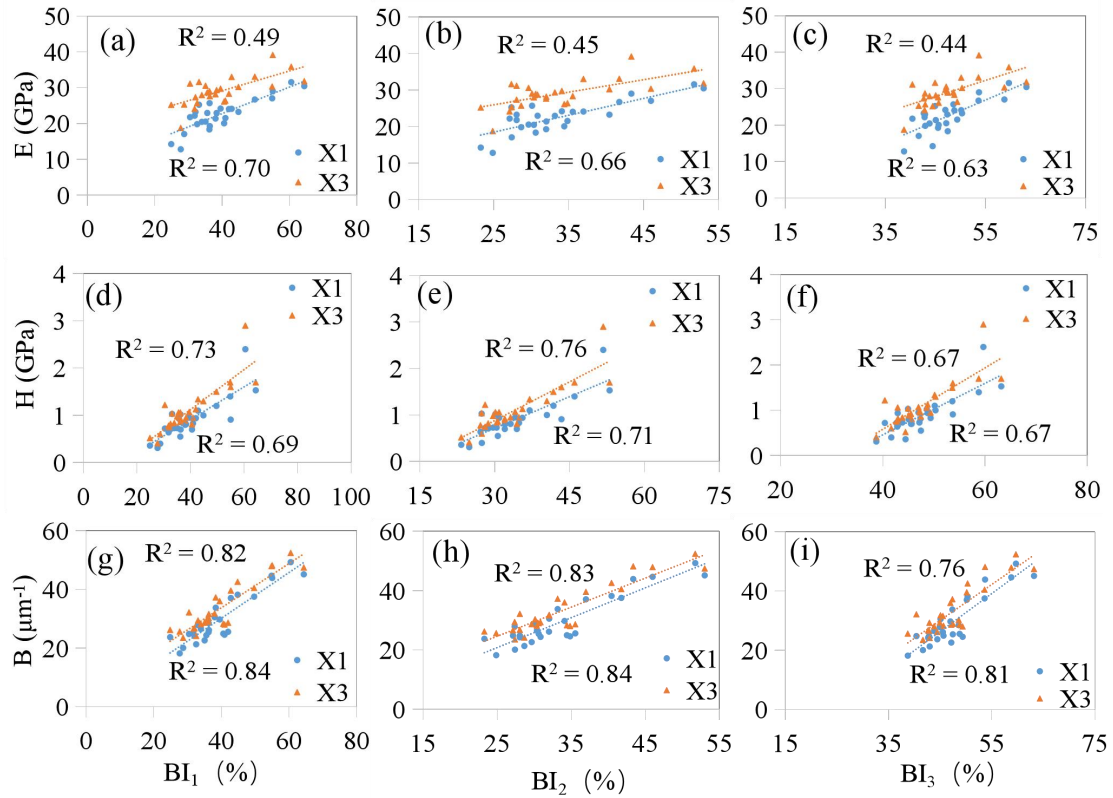
Figure 12. Relationship between Young's modulus (E), hardness, (H), brittleness index (B) based

on the micromechanical properties and brittleness index (BI_1, BI_2, and BI_3) based on mineral

composition of shale

5.3 Relationship between micromechanical properties and sedimentary environment

For all studied shale samples, they were all deposited in a passive continental margin

environment, the depositional period was mainly characterized by a warm and humid climate.

Therefore, these factors are not the main reasons for the change in micromechanical properties of

WF-LMX shales. However, changes in constituents (e.g., organic matter and biogenic silica), and

redox conditions may have a significant effect on the variations in micromechanical properties of

the shales. Previous studies have reported stratigraphic variations in mechanical properties of

shales associated with different rock mineralogy, which resulted from sea level cycles (Harris et

652 al., 2011, Slatt and Abousleiman 2011), and were determined by the sedimentary environment.

653 The WF Formation shales are located in a deep-water continental shelf sedimentary environment.

654 They are located on a transgressive surface of erosion (TSE) or sequence boundary (SB) (Zheng et

655 al., 2018). A decrease in clay minerals and an increase in organic matter and biogenic silica

656 (excess SiO_2) were observed in the transgressive system tract (TST) of the WF Formation from the

657 lower to the upper part, which is likely due to the change in relative sea level and sediment supply

658 (Liu et al., 2019a). Young's modulus, hardness, and brittleness increase in the TST. The increase in

659 diagenetic silica upward through the TST is also found in the Devonian gas shales of the

660 Appalachian Basin, which increases the brittleness (Lash and Blood 2011). The Young's modulus,

661 hardness and brittleness increase almost throughout the TST until reaching up to the maximum

662 flooding surface (MFS), and then decrease slightly in the highstand systems tract (HST) (Figures 6

663 and 7).

664   The lower section of the LMX Formation primarily occupies a deep-water continental shelf,

665 characterized by low-energy and strong reduction conditions, resulting in the deposition of mainly

666 gray-black shale. During the later stages of sedimentation in the LMX Formation, the sea level

667 dropped, and the sedimentary environment gradually shifted to oxidizing conditions and turbidite

668 sediments, leading to the development of a lithological combination dominated by sandy

669 mudstone and muddy siltstone (Figure 1). The LMX Formation locates on a relatively thin

670 carbonaceous shale TST (at the bottom of Rhudianian stage), thicker lowstand systems tract (LST)

671 and highstand systems tract (HST). In general, organic matter and biogenic silica (quartz) decrease

672 sharply from the basal to the upper intervals of Rhudianian stage of the LMX Formation, while

673 they decrease slightly in the LST of Aeronian stage in the LMX Formation. Similarly, there is a

674 decrease in Young's modulus, hardness and brittleness in the HST, followed by a slight decrease in

675 the LST. The HST in the LMX Formation records a large decrease in biogenic silica and organic

676 matter input, which contributes to the decrease in hardness and brittleness. In contrast, the LST

677 records a small decrease in silica and an increased flux of terrigenous clay minerals, resulting in a

678 lower hardness and brittleness (Figures 6 and 7). In general, the elevated values of Young's

679 modulus, hardness and brittleness values are in the middle upper part of the TST in the Katian

680 stage, the HST, the TST in the Hirnantian stage and the bottom part of the HST in the Rhudianian

681 stage, which belong to the deep-water shelf facies, corresponding to a high content of biogenic

682 silica and organic matter, which may be the optimal intervals for hydraulic stimulation in these

683 areas.

684

685 **6. Conclusions**

686   In this paper, we applied nanoindentation mechanical testing along with rock mineralogical,

687 major elemental, and pore analyses to quantitatively evaluate the mechanical profile of WF-LMX

688 shales, and the relationship between micromechanical properties and the sedimentary conditions

689 of marine shale Formation from the WF-LMX member in the shallow SQ-1 well, Sichuan Basin,

690 Southwest China. The results were as follows:

691   (1) The WF-LMX shales within the study region were deposited in a passive margin

692 environment. Biogenic silica was the major source of quartz mineral.

693   (2) The micromechanical properties varied synchronously with mineral and organic content

694 across the vertical drilling profile, reflecting changes in lithology and sedimentary conditions

695 within the WF-LMX Formations. Specifically, in the SQ-1 well, the micromechanical properties

696   of the shales in the WF-LMX Formation exhibit a distinct vertical pattern from bottom to top,

697   sequentially passing through low, high, and low intervals. This pattern is relatively consistent with

698   the variation of quartz and TOC content. However, it is opposite to the pattern of clay mineral

699   content. We interpret these different trends as essentially dominated by the sedimentary

700   environment of shale.

701   (3) Young's modulus shows a positive linear correlation with quartz content and TOC content,

702   and a negative linear correlation with clay minerals, clay+TOC content. There are no or weak

703   correlations with other individual minerals or porosity, suggesting that the micromechanical

704   properties of LMX shale are primarily controlled by quartz content, clay minerals, and organoclay

705   complexes. Autochthonous quartz contributes significantly to the elevated bulk Young's modulus

706   values of the shale.

707   (4) The mineral content/Young's modulus relationship shows a stronger correlation in the X1

708   plane compared to the X3 plane, and the influence of components in shale on hardness or fracture

709   toughness is equivalent to that of Young's modulus.

710   (5) The mineralogy-based brittleness index exhibits a good positive linear correlation with

711   both Young's modulus and hardness, with a slightly better correlation observed for hardness.

712   Besides, the brittleness index based on micromechanical properties shows a significant

713   consistency with the index based on mineral composition. Based on the nanoindentation method,

714   the lower section of the LMX Formation and upper section of the WF Formation, belonging to the

715   deep-water shelf facies, have high brittleness index values, potentially making them ideal intervals

716   for hydraulic stimulation in relevant areas.

717   Our observations here demonstrate the relationship between micromechanical properties and

718   sedimentary environment of WF-LMX shale, and predict the optimal intervals for hydraulic

719   stimulation of WF-LMX shale by the brittleness index based on micromechanical properties.

720   Future research can verify the effectiveness of micromechanics in predicting shale fracture

721   intervals by actual field logging data, such as dynamic Young's modulus, thus expanding the

722   application scope of micromechanics in this field.

723

724 Acknowledgements

725   This research was supported by the China Postdoctoral Science Foundation (2024M763277),

726   the Postdoctoral Fellowship Program of CPSF (Grant No. GZC20241735), the Natural Science

727   Foundation of Guangdong Province (Grant No. 2023A1515030280), the National Natural Science

728   Foundation of China (Grant No. 41802165 and Grant No. 42272182), the Basic and Applied Basic

729   Research Project of Guangzhou City (Grant No. 2023A04J0208), and the Open Fund of Key

730   Laboratory of Petroleum Resources Research, Gansu Province (SZDKFJJ2023009). The authors

731   also thank Dr. Joanna Dziadkowiec and Prof. François Renard who for discussions. This is

732   contribution No.IS-3669 from GIGCAS.

733

734 Declaration of competing interest

735   The authors declare that they have no known competing financial interests or personal

736   relationships that could have appeared to influence the work reported in this paper.

737

738 Data availability

739   The data that support the findings of this study are available from the corresponding author

740   upon reasonable request.

741

Disclaimer

745

Author contributions

747   JW and CY were responsible for the design and methodology of the study, performed the

748 experiments, assembled and analyzed the data, obtained and managed financial support, drafted

749 and revised the paper. YL, WJ, YZ, and YL performed the experiments. YZ, QH, LF, YW, and YL

750 collected the data. TZ, PP, and YX revised the draft. All authors contributed to the review of the

751 article.

752

References

754 Abedi, S., Slim, M., and Ulm, F.-J.: Nanomechanics of organic-rich shales: the role of thermal

755   maturity and organic matter content on texture. Acta Geotech., 11, 775-787.

756   doi:10.1007/s11440-016-0476-2, 2016.

757 Adachi, M., Yamamoto, K., and Sugisaki, R.: Hydrothermal chert and associated siliceous rocks

758   from the northern Pacific their geological significance as indication od ocean ridge activity.

759   Sediment. Geol., 47, 125-148. doi:https://doi.org/10.1016/0037-0738(86)90075-8, 1986.

760 Alramahi, B., and Sundberg, M. I.: Proppant Embedment And Conductivity of Hydraulic

761   Fractures In Shales. Paper presented at the 46th U.S. Rock Mechanics/Geomechanics

762   Symposium, 2012.

763 Boström, K., Kraemer, T., and Gartner, S.: Provenance and accumulation rates of opaline silica, Al,

764   Ti, Fe, Mn, Cu, Ni and Co in Pacific pelagic sediments. Chem. Geol., 11, 123-148.

765   doi:https://doi.org/10.1016/0009-2541(73)90049-1, 1973.

766   Boström, K., and Peterson, M. N. A.: The origin of aluminum-poor ferromanganoan sediments in

767   areas of high heat flow on the East Pacific Rise. Mar. Geol., 7, 427-447.

768   doi:https://doi.org/10.1016/0025-3227(69)90016-4, 1969.

769   Boynton, W.: Cosmochemistry of the Rare Earth Elements: Meteorite Studies. In D. i.

770   Geochemistry (Ed.), 2, pp. 63-114. https://doi.org/10.1016/B978-0-444-42148-7.50008-3,

771   1984.

772   Charlton, T., Rouainia, M., Aplin, A., Fisher, Q., and Bowen, L.: Nanoindentation of Horn River

773   Basin Shales: The Micromechanical Contrast Between Overburden and Reservoir Formations.

774   J. Geophys. Res.: Solid Earth, 128, e2022JB025957. doi:10.1029/2022JB025957, 2023.

775   Chen, X., Fan, J., Chen, Q., Tang, L., and Hou, X.: Toward a stepwise Kwangsian Orogeny.

776   Science China Earth Sci. 57, 379-387. doi:10.1007/s11430-013-4815-y, 2014.

777   Cheng, Y. T., Li, Z., and Cheng, C. M.: Scaling relationships for indentation measurements. Philos.

778   Mag. A, 82, 1821-1829. 2002.

779   Cullers, R., and Podkovyrov, V.: Geochemistry of the Mesoproterozoic Lakhanda shales in

780   southeastern Yakutia, Russia: Implications for mineralogical and provenance control, and

781   recycling. Precambrian Res., 104, 77-93. doi:10.1016/S0301-9268(00)00090-5, 2000.

782   Curtis, M. E., Cardott, B. J., Sondergeld, C. H., and Rai, C. S.: Development of organic porosity in

783   the Woodford Shale with increasing thermal maturity. Int. J. Coal Geol., 103, 26-31.

784   doi:https://doi.org/10.1016/j.coal.2012.08.004, 2012.

785   Cox, R., Lowe, D., and Cullers, R.: The influence of sediment recycling and basement

786   composition on evolution of mudrock chemistry in the southwestern United States. Geochim.

787   Cosmochim. Acta, 59, 2919-2940. doi:10.1016/0016-7037(95)00185-9, 1995.

788   Diao, H.: Rock mechanical properties and brittleness evaluation of shale reservoir. Acta Petro. Sin.,

789   29, 3300-3306. 2013.

790   Du, J., Whittle, A. J., Hu, L., Divoux, T., and Meegoda, J. N.: Characterization of meso-scale

791   mechanical properties of Longmaxi shale using grid microindentation experiments. J. Rock

792   Mech. Geotech. Eng., 13, 555-567. doi:10.1016/j.jrmge.2020.09.009, 2021.

793   Fedo, C., Nesbitt, H., and Young, G.: Unraveling the effects of potassium metasomatism in

794   sedimentary rocks and paleosols, with implications for paleoweathering conditions and

795   provenance.   Geology,   23,   921-924.

796   doi:10.1130/0091-7613(1995)023<0921:UTEOPM>2.3.CO;2, 1995.

797   Fender, T. D., Van Der Land, C., Rouainia, M., Graham, S. P., Jones, D. M., Vane, C. H., and

798   Wagner, T.: The Assessment of Organic Matter Young's Modulus Distribution With

799   Depositional Environment and Maturity. J. Geophys. Res.: Solid Earth, 125, e2020JB020435.

800   doi:10.1029/2020jb020435, 2020.

801   Gautham, S., and Sasmal, S.: Nano-scale fracture toughness of fly ash incorporated hydrating

802   cementitious composites using experimental nanoindentation technique. Theor. Appl. Fract.

803   Mech., 117, 103180. doi:https://doi.org/10.1016/j.tafmec.2021.103180, 2022.

804   Glorioso, J. C., and Rattia, A.: Unconventional reservoirs: basic petrophysical concepts for shale

805   gas. Paper presented at the SPE. 153004, pp. 1-38, 2012.

806   Guo, T., and Zeng, P.: The Structural and Preservation Conditions for Shale Gas Enrichment and

807   High Productivity in the Wufeng — Longmaxi Formation, Southeastern Sichuan Basin.

808   Energy Explor. Exploit., 33, 259-276. 2015.

809   Guo, T., Zhang, S., Qu, Z., Zhou, T., Xiao, Y., and Gao, J.: Experimental study of hydraulic

810   fracturing   for   shale   by   stimulated   reservoir   volume.   Fuel,   128,   373-380.

811   doi:https://doi.org/10.1016/j.fuel.2014.03.029, 2014.

812   Guo, W., Shen, W., Li, X., Wang, N., Liu, X., Zhang, X., and Zhou, S.: Study on mechanical

813   characteristics and damage mechanism of the Longmaxi Formation shale in southern Sichuan

814   Basin, China. Energy Explor. Exploit., 38, 454-472. doi:10.1177/0144598719876858, 2019.

815   Gupta, I., Sondergeld, C., and Rai, C.: Applications of NanoIndentation for Reservoir

816   Characterization in Shales. In 52nd US Rock Mechanics/Geomechanics Symposium. 2018.

817   Gupta, I., Sondergeld, C., and Rai, C.: Fracture toughness in shales using nano-indentation. J.

818   Petro. Sci. Eng., 191, 107222. doi:10.1016/j.petrol.2020.107222, 2020.

819   Harris, N., Miskimins, J., and Mnich, C.: Mechanical anisotropy in the Woodford Shale, Permian

820   Basin: Origin, magnitude, and scale. The Leading Edge, 30, 284-291. doi:10.1190/1.3567259,

821   2011.

822   He, C., Ji, L., Wu, Y., Su, A., and Zhang, M.: Characteristics of hydrothermal sedimentation

823   process in the Yanchang Formation, south Ordos Basin, China: Evidence from element

824   geochemistry. Sediment. Geol., 345, 33-41. doi:https://doi.org/10.1016/j.sedgeo.2016.09.001,

825   2016.

826   Jarvie, D., Hill, R., Ruble, T., and Pollastro, R.: Unconventional shale-gas systems: The
827   Mississippian Barnett Shale of north-central Texas as one model for thermogenic shale-gas
828   assessment. AAPG bulletin, 91, 475-499. doi:10.1306/12190606068, 2007.

829   Jia, L., Xu, Q., and Zhang, L.: Assessment of deep shale fracture toughness using nanoindentation
830   tests. IOP Conf. Ser.: Earth Environ. Sci, 861, 062068. doi:10.1088/1755-1315/861/6/062068,
831   2021a.

832   Jia, Y., Tang, J., Lu, Y., and Lu, Z.: Laboratory geomechanical and petrophysical characterization
833   of Longmaxi shale properties in Lower Silurian Formation, China. Mar. Pet. Geol., 124,
834   104800. doi:https://doi.org/10.1016/j.marpetgeo.2020.104800, 2021b.

835   Kumar, V., Sondergeld, C. H., and Rai, C. S.: Nano to Macro Mechanical Characterization of
836   Shale. Paper presented at the In SPE annual technical conference and exhibition, SPE 159804.
837   https://doi.org/10.2118/159804-MS, 2012.

838   Larsson, P. L., Giannakopoulos, A. E., Sderlund, E., Rowcliffe, D. J., and Vestergaard, R.:
839   Analysis of Berkovich indentation. International Journal of Solids & Structures, 33, 221-248.
840   doi:10.1016/0020-7683(95)00033-7, 1996.

841   Lash, G., and Blood, R.: Sequence stratigraphy as expressed by shale source rock and reservoir
842   characteristics—Examples from the Devonian succession, Appalachian Basin. AAPG Search
843   and Discovery, 80168. 2011.

844   Laugier, M. T.: Palmqvist indentation toughness in WC-Co composites. J. Mater. Sci. Lett., 6,
845   897-900. doi:10.1007/BF01729862, 1987.

846   Lawn, B. R., and Marshall, D. B.: Hardness, Toughness, and Brittleness: An Indentation Analysis.
847   J. Am. Ceram. Soc., 62, 347-350. doi:https://doi.org/10.1111/j.1151-2916.1979.tb19075.x,
848   1979.

849   Li, C., Ostadhassan, M., Abarghani, A., Fogden, A., and Kong, L.: Multi-scale evaluation of
850   mechanical properties of the Bakken shale. J. Mater. Sci., 54, 2133-2151.
851   doi:10.1007/s10853-018-2946-4, 2018.

852   Li, H., Li, D., He, Q., Sun, Q., and Zhao, X.: Controlling mechanism of shale palaeoenvironment
853   on its tensile strength: A case study of Banjiuguan Formation in Micangshan Mountain. Fuel,
854   355, 129505. doi:https://doi.org/10.1016/j.fuel.2023.129505, 2024.

855   Li, Y., Zhang, T., Ellis, G. S., and Shao, D.: Depositional environment and organic matter

856   accumulation of Upper Ordovician – Lower Silurian marine shale in the Upper Yangtze

857   Platform, South China. Palaeogeogr. Palaeoecl., 466, 252-264.

858   doi:https://doi.org/10.1016/j.palaeo.2016.11.037, 2017.

859 Liu, B., Schieber, J., Mastalerz, M., and Teng, J.: Organic matter content and type variation in the

860   sequence stratigraphic context of the Upper Devonian New Albany Shale, Illinois Basin.

861   Sediment. Geol., 383, 101-120. doi:https://doi.org/10.1016/j.sedgeo.2019.02.004, 2019a.

862 Liu, K., Jin, Z., Zeng, L., Ostadhassan, M., and Xu, X.: Understanding the creep behavior of shale

863   via nano-DMA method. Energy Rep., 7, 7478-7487.

864   doi:https://doi.org/10.1016/j.egyr.2021.10.099, 2021.

865 Liu, K., Jin, Z., Zeng, L., Ozotta, O., Gentzis, T., and Ostadhassan, M.: Alteration in the

866   mechanical properties of the Bakken during exposure to supercritical $CO2$. Energy, 262,

867   125545. doi:https://doi.org/10.1016/j.energy.2022.125545, 2022.

868 Liu, K., Ostadhassan, M., and Bubach, B.: Applications of nano-indentation methods to estimate

869   nanoscale mechanical properties of shale reservoir rocks. J. Nat. Gas Sci. Eng., 35,

870   1310-1319. doi:10.1016/j.jngse.2016.09.068, 2016.

871 Liu, Y.: Fracture toughness assessment of shales by nanoindentation. MS Thesis. University of

872   Massachusetts Amherst. Cambridge, 2015.

873 Liu, Y., Xiong, Y., Liu, K., Yang, C., and Peng, P.: Indentation size and loading rate sensitivities on

874   mechanical properties and creep behavior of solid bitumen. Int. J. Coal Geol., 216, 103295.

875   doi:https://doi.org/10.1016/j.coal.2019.103295, 2019b.

876 Long, Y., Zhang, Y., Huang, X., Wang, Y., Zhao, Y., Wang, R., and Song, F.: Assessment of the

877   Multiphase Mechanical Properties of the Longmaxi Formation Shale Using Nanoindentation

878   Tests. ACS Omega, 6, 18200-18214. doi:10.1021/acsomega.1c02049, 2021.

879 Ma, Y., Zhong, N., Li, D., Pan, Z., Cheng, L., and Liu, K.: Organic matter/clay mineral

880   intergranular pores in the Lower Cambrian Lujiaping Shale in the north-eastern part of the

881   upper Yangtze area, China: A possible microscopic mechanism for gas preservation. Int. J.

882   Coal Geol., 137, 38-54. doi:https://doi.org/10.1016/j.coal.2014.11.001, 2015.

883 Manjunath, G. L., and Jha, B.: Geomechanical characterization of gondwana shale across

884   nano-micro-meso scales. Int. J. Rock Mech. Min. Sci., 119, 35-45.

885   doi:https://doi.org/10.1016/j.ijrmms.2019.04.003, 2019.

886 Maynard, J. B., Valloni, R., & Yu, H.S. Composition of modern deep-sea sands from arc-related

887   basins Geological Society of of London Special Publications, 10, 551–561. 1982.

888 Milliken, K. L., Ergene, S. M., and Ozkan, A.: Quartz types, authigenic and detrital, in the Upper

889   Cretaceous Eagle Ford Formation, South Texas, USA. Sediment. Geol., 339, 273-288.

890   doi:https://doi.org/10.1016/j.sedgeo.2016.03.012, 2016.

891 Murray, R. W., Buchholtz Ten Brink, M. R., Gerlach, D. C., Russ, G. P., and Jones, D. L.: Rare

892   earth, major, and trace elements in chert from the Franciscan Complex and Monterey Group,

893   California: Assessing REE sources to fine-grained marine sediments. Geochim. Cosmochim.

894   Acta, 55, 1875-1895. doi:https://doi.org/10.1016/0016-7037(91)90030-9, 1991.

895 Nesbitt, H., and Wilson, R.: Recent Chemical Weathering of Basalts. Am. J. Sci., 292, 740-777.

896   doi:10.2475/ajs.292.10.740, 1992.

897 Nesbitt, H. W., and Young, G. M.: Early Proterozoic climates and plate motions inferred from

898   major element chemistry of lutites. Nature, 299, 715-717. doi:10.1038/299715a0, 1982.

899 Oliver, W. C., and Pharr, G. M.: An improved technique for determining hardness and elastic

900   modulus using load and displacement sensing indentation experiments. J. Mater. Res., 7,

901   1564-1583. doi:10.1557/JMR.1992.1564, 1992.

902 Oliver, W. C., and Pharr, G. M.: Measurement of hardness and elastic modulus by instrumented

903   indentation: Advances in understanding and refinements to methodology. J. Mater. Res., 19,

904   3-20. 2004.

905 Reimann, C., and de Caritat, P.: New soil composition data for Europe and Australia:

906   Demonstrating comparability, identifying continental-scale processes and learning lessons for

907   global geochemical mapping. Sci. Total Environ., 416, 239-252.

908   doi:https://doi.org/10.1016/j.scitotenv.2011.11.019, 2012.

909 Reynolds, J. H., and Verhoogen, J.: Natural variations in the isotopic constitution of silicon.

910   Geochim. Cosmochim. Acta, 3, 224-234. doi:https://doi.org/10.1016/0016-7037(53)90041-6,

911   1953.

912 Rickman, R., Mullen, M., Petre, E., Grieser, B., and Kundert, D. (2008). A Practical Use of Shale

913   Petrophysics for Stimulation Design Optimization: All Shale Plays Are Not Clones of the

914   Barnett Shale. Paper presented at the SPE Annual Technical Conference and Exhibition.

915   https://doi.org/10.2118/115258-MS

Roser, B. P., and Korsch, R. J.: Provenance signatures of sandstone-mudstone suites determined using discriminant function analysis of major-element data. Chem. Geol., 67, 119-139. doi:https://doi.org/10.1016/0009-2541(88)90010-1, 1988.

Schieber, J., Krinsley, D., and Riciputi, L.: Diagenetic origin of quartz silt in mudstones and implications for silica cycling. Nature, 406, 981-985. doi:10.1038/35023143, 2000.

Sethi, C., Hazra, B., Ostadhassan, M., Motra, H. B., Dutta, A., Pandey, J. K., and Kumar, S.: Depositional environmental controls on mechanical stratigraphy of Barakar Shales in Rajmahal Basin, India. Int. J. Coal Geol., 285, 104477. doi:https://doi.org/10.1016/j.coal.2024.104477, 2024.

Shi, X., He, Z., Long, S., Peng, Y., Li, D., and Jiang, S.: Loading rate effect on the mechanical behavior of brittle longmaxi shale in nanoindentation. Int. J. Hydrogen Energy, 44, 6481-6490. doi:10.1016/j.ijhydene.2019.01.028, 2019a.

Shi, X., Jiang, S., Lu, S., He, Z., Li, D., Wang, Z., and Xiao, D.: Investigation of mechanical properties of bedded shale by nanoindentation tests: A case study on Lower Silurian Longmaxi Formation of Youyang area in southeast Chongqing, China. Pet. Explor. Dev., 46, 163-172. doi:10.1016/s1876-3804(19)30016-3, 2019b.

Shi, X., Jiang, S., Wang, Z., Bai, B., Xiao, D., and Tang, M.: Application of nanoindentation technology for characterizing the mechanical properties of shale before and after supercritical CO_2 fluid treatment. J. CO_2 Util., 37, 158-172. doi:10.1016/j.jcou.2019.11.022, 2020.

Shukla, P., Kumar, V., Curtis, M., Sondergeld, C. H., and Rai, C. S.: Nanoindentation Studies on Shales. Paper presented at the 47th U.S. Rock Mechanics/Geomechanics Symposium, San Francisco, California, 2013.

Slatt, R. M., and Abousleiman, Y.: Merging sequence stratigraphy and geomechanics for unconventional gas shales. The Leading Edge, 30, 274-282. doi:10.1190/1.3567258, 2011.

Sone, H., and Zoback, M. D.: Mechanical properties of shale-gas reservoir rocks — Part 1: Static and dynamic elastic properties and anisotropy. Geophysics, 78, D381-D392. doi:10.1190/geo2013-0050.1, 2013a.

Sone, H., and Zoback, M. D.: Mechanical properties of shale-gas reservoir rocks — Part 2: Ductile creep, brittle strength, and their relation to the elastic modulus. Geophysics, 78, D390-D399. 2013b.

946 Ulm, F.J., and Abousleiman, Y.: The nanogranular nature of shale. Acta Geotech., 1, 77-88.
947   doi:10.1007/s11440-006-0009-5, 2006.

948 Ulm, F. J., Delafargue, A., and Constantinides, G.: Experimental Microporomechanics: Springer
949   Vienna, 2005.

950 Wang, F. P., and Gale, J. F.: Screening criteria for shale-gas systems. Gulf Coast Association of
951   Geological Societies Transactions, 59, 779-793. 2009.

952 Wang, J., Dziadkowiec, J., Liu, Y., Jiang, W., Zheng, Y., Xiong, Y., Peng, P. a., and Renard, F.:
953   Combining atomic force microscopy and nanoindentation helps characterizing in-situ
954   mechanical properties of organic matter in shale. Int. J. Coal Geol., 281, 104406.
955   doi:https://doi.org/10.1016/j.coal.2023.104406, 2024.

956 Wang, J., Yang, C., Liu, Y., and Xiong, Y.: Nanoindentation investigation of mechanical and creep
957   properties of continental Triassic Yanchang Formation shale, Ordos Basin. Interpretation, 10,
958   SJ29-SJ41. https://doi.org/10.1190/int-2021-0218.1, 2022a.

959 Wang, J., Yang, C., Liu, Y., Li, Y., and Xiong, Y.: Using Nanoindentation to Characterize the
960   Mechanical and Creep Properties of Shale: Load and Loading Strain Rate Effects. ACS
961   Omega, 7, 14317-14331. doi:10.1021/acsomega.2c01190, 2022b.

962 Wang, J., Liu, Y., Yang, C., Jiang, W., Li, Y., Xiong, Y., and Peng, P. a.: Evolution of mechanical
963   properties of kerogen with thermal maturity. Mar. Pet. Geol., 145, 105906.
964   doi:https://doi.org/10.1016/j.marpetgeo.2022.105906, 2022c.

965 Wang, J., Liu, Y., Yang, C., Zheng, Y., Jiang, W., Menegon, L., Renard, F., Peng, P. a., and Xiong,
966   Y.: Upscaling the creep behavior of clay-rich and quartz-rich shales from nanoindentation
967   measurements: Application to the Wufeng-Longmaxi shale, China. Int. J. Rock Mech. Min.
968   Sci., 171, 105580. doi:https://doi.org/10.1016/j.ijrmms.2023.105580, 2023.

969 Wang, Q., Feng, Y., Gao, P., Meng, G., Lu, C., Fan, Q., Li, G., Tan, Y., and Xiao, X.: Influence of
970   the sedimentary environment of the Wufeng-Longmaxi shale on organic matter accumulation
971   in the Dingshan area, Sichuan Basin. Front. Earth Sci., 12, 1457377.
972   doi:10.3389/feart.2024.1457377, 2024.

973 Wei, C., Dong, T., He, Z., He, S., He, Q., Yang, R., Guo, X., and Hou, Y.: Major, trace-elemental
974   and sedimentological characterization of the upper Ordovician Wufeng-lower Silurian
975   Longmaxi formations, Sichuan Basin, south China: Insights into the effect of relative

976   sea-level fluctuations on organic matter accumulation in shales. Mar. Pet. Geol., 126, 104905.

977   doi:10.1016/j.marpetgeo.2021.104905, 2021.

978   Yan, C., Jin, Z., Zhao, J., Du, W., and Liu, Q.: Influence of sedimentary environment on organic

979   matter enrichment in shale: A case study of the Wufeng and Longmaxi Formations of the

980   Sichuan   Basin,   China.   Mar.   Pet.   Geol.,   92,   880-894.

981   doi:https://doi.org/10.1016/j.marpetgeo.2018.01.024, 2018.

982   Yang, C., Xiong, Y., Wang, J., Li, Y., and Jiang, W.: Mechanical characterization of shale matrix

983   minerals using phase-positioned nanoindentation and nano-dynamic mechanical analysis. Int.

984   J. Coal Geol., 229, 103571. doi:10.1016/j.coal.2020.103571, 2020.

985   Yang, Z., Wang, L., Chen, Z., Xiang, D., Hou, D., Ho, C. L., and Zhang, G.: Micromechanical

986   Characterization of Fluid/Shale Interactions by Means of Nanoindentation. SPE Reservoir

987   Eval. Eng, 21, 405-417. doi:10.2118/181833-pa, 2018.

988   Yang, Z., Wang, L., Zhang, G., and Ho, C.: Micromechanical characterization of fluid-shale

989   interactions via nanoindentation. Paper presented at the SPE Asia Pacific Hydraulic

990   Fracturing Conference, 2016.

991   Zeng, Q., Feng, Y., and Xu, S.: A discussion of "Application of nano-indentation methods to

992   estimate nanoscale mechanical properties of shale reservoir rocks" by K Liu, M

993   Osatadhassan   and   B   Bubach.   J.   Nat.   Gas   Sci.   Eng.,   42,   187-189.

994   doi:10.1016/j.jngse.2017.02.027, 2017.

995   Zeng, Q., Wu, Y., Liu, Y., and Zhang, G.: Determining the micro-fracture properties of Antrim gas

996   shale by an improved micro-indentation method. J. Nat. Gas Sci. Eng., 62, 224-235.

997   doi:10.1016/j.jngse.2018.12.013, 2019.

998   Zhao, J., Zhang, D., Wu, T., Tang, H., and Dai, C.: Multiscale Approach for Mechanical

999   Characterization of Organic-Rich Shale and Its Application. Int. J. Geomech., 19, 04018180.

1000   2019.

1001   Zhao, X., Li, Q., Jiang, Z., Zhang, R., and Li, H.: Organic geochemistry and reservoir

1002   characterization of the organic matter-rich calcilutite in the Shulu Sag, Bohai Bay Basin,

1003   North   China.   Mar.   Pet.   Geol.,   51,   239-255.

1004   doi:https://doi.org/10.1016/j.marpetgeo.2013.12.014, 2014.

1005   Zheng, Y., Liao, Y., Wang, Y., Xiong, Y., and Peng, P. a.: Organic geochemical characteristics,

1006   mineralogy, petrophysical properties, and shale gas prospects of the Wufeng – Longmaxi

1007   shales in Sanquan Town of the Nanchuan District, Chongqing. AAPG Bull., 102, 2239-2265.

1008   doi:10.1306/04241817065, 2018.

1009 Zheng, Y., Liao, Y., Wang, Y., Xiong, Y., and Peng, P. a.: The main geological factors controlling

1010   the Wufeng-Longmaxi shale gas content. AAPG Bull., 106, 2073-2102.

1011   doi:10.1306/07132218243 %J AAPG Bulletin, 2022.

1012 Zou, C., Dong, D., Wang, S., Li, J., Li, X., Wang, Y., Li, D., and Cheng, K.: Geological

1013   characteristics and resource potential of shale gas in China. Pet. Explor. Dev., 37, 641-653.

1014   doi:10.1016/s1876-3804(11)60001-3, 2010.

1015